1    **The impact of mineral compositions on hydrate morphology evolution and phase**

2    **transition hysteresis in natural clayey silts**

3    Hang Bian [a,b], Xuwen Qin [c,d,e], Jinsheng Sun [f,g], Wanjing Luo [a*], Cheng Lu [b,d,e], Jian Zhu [h], Chao Ma [d,e],

4    Yingfang Zhou [a,i*]

5    a. School of Energy Resources, China University of Geosciences, Beijing 100083, China

6    b. Center of Oil & Natural Gas Resource Exploration, China Geological Survey, Beijing 100083, China

7    c. China Geological Survey, Beijing 100083, China

8    d. Guangzhou Marine Geological Survey, China Geological Survey, Guangzhou 510075, China

9    e. National Engineering Research Center of Gas Hydrate Exploration and Development, Guangzhou 511458,

10    China

11    f. China University of Petroleum (East China), Qingdao 266580, China

12    g. CNPC Engineering Technology R&D Company Limited, Beijing 102206, China

13    h. iRock Technologies, Beijing 100094, China

14    i. School of Engineering, University of Aberdeen, UK

15    Correspondence should be addressed to Wanjing Luo luowanjing@cugb.edu.cn

16    and Yingfang Zhou Yingfang.zhou@abdn.ac.uk

17    **Abstract**

18    Natural gas hydrate is a clean and high-efficient energy resource, and more than 90% of its reserves

19    are contained in fine-grained (typically clayey silts) sediment. In this work, for the first time, the

20    micro-scale imaging is performed to explore hydrate phase transition, morphology evolution and

21    fundamental characteristics (mineral compositions, pore structures and seepage capacity) in clayey

22    silt sediments. The results indicate that clayey silts formation properties strongly depend on

23  dominant minerals component in the sediments. The clay-rich clayey silt possesses more

24  microcapillary interstice with smaller permeability than that in quartz-rich sediment. Hydrates

25  generally occur as microfracture-filling (veins) and grain-displacing (nodulus) in sand-rich clayey

26  silt. While they occur in the form of fracture-filling (vein) and foraminifera-filling in clay-rich

27  clayey silt sediments. Biological fossils (especially foraminifera) provides potential space for

28  hydrate aggregates. But hydrate formed inside it depends on the structures of fossils, the mineral

29  components and pore structure of surrounding matrix. The hysteresis between hydrate formation

30  and decomposition found to be more significant in clary-rich clayey silt sediment than quartz-rich

31  sediment. And this hysteresis inside foraminifera is much more serious compared with that in matrix.

32  In addition, dispersed pore-filling hydrates forms during decomposition, which has adverse effect

33  on continuous gas production.

34  **Keywords:** Clayey silt, Hydrate phase transition, Micro-scale properties, Micro-scale imaging

35

## 1. Introduction

37  Under the background of economic globalization, the global energy consumption is projected to

38  increase in the coming years [1]. However, carbon emission from the conventional fossil fuels has

39  led to increasing environmental concern and global warming, which becomes an imminent

40  consideration [2]. NGHs is crystalline solid, in which guest gas molecules are trapped in host water

41  cavities [3]. NGH is widely distributed in continental permafrost and marine sediments, and it is

42  considered as an environmental-friendly alternative energy resource compared with other fossil

43  fuels [4]. The estimated global natural hydrate reserve is twice of that in combined conventional

44  fossil fuels [3]. The promising prospect has arisen great interests of energy consuming countries in

45 recent years and many of them have carried out geological explorations [5] or pilot field tests [6].

46 According to statistics, hydrate in clayey silt sediments contains more than 90% of the total NGH

47 resources in the world [7,8]. Typical clayey-silt hydrate reservoirs are globally distributed, including

48 the Ulleung Basin in Korea [9], the northern part of the South China Sea [10], the Gulf of Mexico

49 [11,12], the Cascadia Margin [13], the offshore Peru [14,15] and the K-G Basin in India [16], etc.

50 Thoughtful understanding of hydrate formation and decomposition process, such as hydrate

51 morphology, hydrate phase transition and the evolution of them can provide strong theoretical

52 support for better NGH development. The attenuation of P- and S-waves and change of conductivity

53 during seismic exploration and resource assessment is directly governed by hydrate structure and

54 saturation in NGH reservoir [17-22]. In addition, the physical properties of hydrate-bearing

55 sediments, such as thermal conductivity [23], intrinsic permeability [24] and mechanical strength

56 [25] are also dominated by the specific distribution of hydrates in porous medium.

57 With the recent development of imaging technologies, micro-CT has been widely used as a

58 nondestructive instrument to observe the inner structure of hydrate-bearing samples [26]. Numerous

59 scholars have conducted research on hydrate formation and decomposition process based on CT

60 technology. For hydrate formation, most of the scholars [27-30] found that hydrates preferentially

61 developed at gas-water interface. Hydrates possess irregular microstructures [30], and the nucleation

62 and distribution of hydrates are heterogeneous at grain scale as well as sample scale [28,31]. The

63 distribution and migration of gas and water phases dominate the subsequent growth direction [31]

64 and surface morphology of hydrates [28,31]. Specifically, Lei et al. [33] indicated that hydrate

65 tended to adopt round and smooth surfaces when in contact with water, while exhibited angular

66 interfaces when in contact with gas. Moreover, gas occurrence types can also alter hydrate

67    occurrences [34].

68    For hydrate decomposition, some scholars indicated that hydrate decomposition started at the

69    hydrate-gas interface, not at the contacts with quartz grains [6,35]. Gupta et al. [36] confirmed the

70    characteristic of radial dissociation of hydrates. The different changing rate of hydrate surface area

71    at different decomposition stages suggests that hydrate morphology will change during

72    decomposition [37]. Some scholars indicated that this hydrate morphology transition is caused by

73    the change of the distribution of decomposed water [35] and the limited diffusion of gas in water

74    phase [38]. Moreover, hydrate re-formation was likely to occur during initial decomposition process

75    [35]. And water saturation was the dominant factor of hydrate re-formation site [39].  Meanwhile

76    the hydrate re-formation may promote homogeneous distribution of hydrate in pores [6].

77    The distinction between different hydrate habits (cementing or non-cementing) was initially

78    deduced from the effect of hydrate morphologies on elastic wave velocity [40]. Several idealistic

79    theoretical models (including pore-filling, grain-cementing, grain-coating, load-bearing and patchy)

80    for pore habits of laboratory-synthesized hydrates in porous medium have been proposed in previous

81    literatures [41-45]. Some researchers have conducted the studies on hydrate pore habits evolution

82    based on micro-CT technology. Results show that different hydrate formation conditions (such as

83    excess-gas and excess-water) can lead to different evolution rules of hydrate habits [31, 33]. Mass

84    and heat transfer during hydrate formation can also lead to habit transformation.

85    However, it is worth noting that the above-mentioned studies were conducted in large size (hundreds

86    to thousands of microns) glass beads or quartz sand, which are the experimental substitutes of

87    coarse-grained hydrate sediments. These materials are enormously different from the natural fine-

88    grained clayey silt hydrate sediments in mineral composition, particle size distribution, types of

89 porous space and seepage capacity. The natural clayey silt hydrate sediments possess typical

90 characteristics of tight reservoirs, including extremely small pore size, low porosity and ultra-low

91 permeability [46]. Numerous field coring data indicate that hydrates in coarse-grained sediments

92 basically show the same hydrate occurrence as those observed in large-grained glass beads or quartz

93 sands in laboratory tests. While the hydrate occurrences in fine-grained sediments (typically clayey

94 silts) mainly show in grain-displacing occurrence (including fracture-filling/ veins, chunks/nodules

95 and lenses types), which are significantly different from those in coarse-grained sediments [47,48].

96 The essence of the difference is that further hydrate growth mostly proceeds by invading adjacent

97 pores in coarse-grained sediment when hydrate growth is restricted by mineral particles; While in

98 fine-grained sediment, further hydrate growth is mainly achieved by replacing particles to enlarge

99 the occupied pores [41]. It is mainly caused by the relative balance between the effective stress and

100 the hydrate-water capillarity in sediments with difference particle sizes. Capillary force prevails in

101 fine-grained sediment, so that hydrate is easier to replace particles than to invade into small throats.

102 The pore throats size of coarse sediment is much larger and the capillary force is insignificant.

103 Therefore, hydrate is more inclined to invade the adjacent pores under high effective stress [41].

104 By far, there has been limited lab study on hydrates in natural clayey silt at micro-scale. Wu et al.

105 observed hydrate occurrences in silty sediment and discussed mechanical properties of hydrate-

106 bearing clayey silt by self-developed CT triaxial apparatus [49]. Liu et al. [50] conducted nano-CT

107 scanning on samples from Shenhu area in the South China Sea and found that clayey silts are usually

108 rich in foraminifera, which increases pore space of sediments. Liu et al. [51] performed X-CT

109 scanning on natural hydrate-bearing clayey silt pressure-core at low-temperature and high-pressure

110 condition. Results indicated that there were only bulk hydrates formed in clayey silt without bio-

111     fossils, and no dispersed hydrates were found in matrix pores. Li et al. [52] synthesized hydrate in

112     foraminifera and demonstrated that liquid and gas migrated into the shells through through-holes

113     and hydrates directly contacted inner wall of foraminifera. At present, there is few research on

114     evolution of hydrate occurrences in fine-grained sediments, and even less research on the

115     characteristics of hydrate phase transition in such sediments.

116     The overall aim of this work is to investigate the characteristics of hydrate phase transition and

117     morphology evolution in clayey silts. Two representative clayey silts with difference dominant

118     minerals collected from the hydrate reservoir in the South China Sea are selected by quantitative

119     characterization through QEMSCAN technology. Quantitative characterizations of particle size,

120     pore space and seepage capacity are performed based on the obtained multi-scale spatial structures

121     of samples by SEM and micro-CT scanning techniques.  Similar to the previous study [53], xenon

122     is utilized as a substitute of methane to generate hydrate in this study. Hydrate phase transition

123     experiments in natural clayey silts are successfully performed by using stepwise pressurization and

124     depressurization methods for the first time. The pore-scale distribution and morphology evolution

125     of hydrate at typical states during formation and decomposition are captured. The decisive effect of

126     mineral compositions on the phase transition properties and morphology evolutions has been

127     discussed contrastively. The results of this research are the theoretical basis of studies on evolution

128     characteristics of seepage capacity and mechanical properties during hydrate phase transition in

129     clayey silts. In addition, the results possesses guiding significance to the production tests of clayey

130     silt hydrate-bearing reservoirs.

131     **2.   Sample preparation and methodology**

132     **2.1   Dry scan of clayey silt samples**

133     As observed in the field, the contents of silt and clay vary significantly in different fine-grained

134 NGH sediments. For example, the overall sand content is lower in the K-G basin of India, but some

135 high-concentrated sand regions can still be observed [54]. In Ulleung Basin, mineral contents of the

136 sandy clay sediment are different from those in the clay-dominant fine-grained sediments [55]; and

137 there are many microfossils dispersing in clay minerals in the clay-dominant sediments. In the South

138 China Sea, the sand content in clayey silt sediment of Qiong Dongnan area is higher than that of

139 Shenhu area [56,57]. While the clay content of the sediments in the offshore Peru, the Gulf of

140 Mexico and the Cascadia Margin are generally dominant [41]. Previous work also suggests

141 classifying the fine-grained NGH sediments into three main lithofacies with distinct grain size

142 distributions (type-A-silty clay to clayey silt, Type B-clayey silt and Type C-sandy silt to silty sand),

143 indicating that grain size increases with the decrease of clay content [58]. And thus, two typical

144 samples (clay-rich and sand-rich clayey silt natural hydrate sediments) were selected as example to

145 analyze the hydrate occurrence evolution in clayey silt hydrate reservoir. Before phase transition

146 experiments, the two samples are scanned by several methods to provide basic images for the

147 subsequent qualitative and quantitative characterization of physical properties including mineralogy,

148 pore space and seepage capacity. The specific preparation process of SEM samples is detailed in

149 Appendix A.

150 **MAPS imaging.** Scanning electron microscope (SEM) is an instrument for high-resolution imaging

151 of materials [59]. The electrons interact and scatter as impacting various minerals. SEM images can

152 be obtained by scanning the surface of specimen and mapping the intensity of corresponding

153 scattered electrons and other energy signals [60]. The primary electrons reflected by elastic

154 collisions, also known as backscattered electrons (BSE), is one of the main parts of the imaging

155 signal in SEM. The electrons are converted into video signals through the detector and the SEM

156 image can be formed after amplification and brightness adjustment.

157 MAPS is a modular automated processing system with automatic imaging control function. It can

158 seamlessly stitch thousands of high-resolution SEM images together to generate a complete, multi-

159 scale SEM image of the area of interest. In this study, MAPS images of the target areas are acquired

160 by stitching plenty of consecutive SEM images with a resolution of 5μm and pixel number of 2048

161 ×1768.

162 **QEMSCAN imaging.** QEMSCAN (Quantitative Evaluation of Minerals by Scanning electron

163 microscopy) is a comprehensive automatic mineral detection method. QEMSCAN technology

164 combines energy-dispersive spectroscopy (EDS) and backscattered electron (BSE) intensity from a

165 SEM and identifies minerals by comparison with a pre-defined mineral database [61]. The specific

166 descriptions are referred in the research of Gottlieb et al. [62]. In this work, a 15kV electron beam

167 is used to obtain 2D SEM images for quantitative analysis of minerals in a high vacuum condition.

168 The scanning resolution is 5μm, and the scanning area is 8 mm × 8 mm. A series of data processing

169 is then performed, specifically including integrating several mineral phases into mineral aggregates,

170 decomposing mixed spectra (boundary phase processing), image filtering, and particle classification.

171 **FIB-SEM imaging.** FIB-SEM (Focused Ion Beam Scanning Electron Microscopy) is the

172 combination of SEM and focused ion beam [63,64]. Firstly, the 3D slice range and thickness

173 (number of slices) are set. After scanned by electron beam, the sample surface is etched by the large

174 focused ion beam and then smoothed by the small one. Subsequently, SEM scans the new sample

175 surface [65]. This cycle continues until the sample is cut to a predetermined depth. Finally, plenty

176 of continuous 2D images are reconstructed into 3D FIB-SEM images using reconstruction algorithm.

177 **Micro-CT imaging.** 3D internal space of samples can also be tested by micro-computed

178 tomography (micro-CT), which is a non-destructive technology. The high-pressure chamber is fixed

179 on the 3D detection platform, and rotates 360° for scanning [53]. The radiation emitted from X-ray

180 source is attenuated by various phases and then received by the detector. To optimize image quality,

181 each sample is scanned under 120kV. By converting the attenuated X-rays into digital and electrical

182 signals, the attenuation coefficients are acquired, and 3D gray-scale images of the samples can be

183 subsequently obtained by 3D reconstruction algorithm [53].

184 **2.2  Hydrate phase transition experiment**

185 **Experimental preparations.** A cylinder with a length of 4mm and a diameter of 5mm are sampled

186 from each of the two pieces for hydrate phase transition experiment. Xenon gas (purity of 99.999%)

187 and the in-situ seawater produced by thawing frozen samples serve as raw materials of hydrate

188 formation. Both methane hydrate and xenon hydrate are classified as Type I structure hydrate [66].

189 The similarities of the two hydrates in various aspects have been verified, including lattice structure,

190 phase equilibrium thermodynamic, growth kinetics and mechanical properties [67-69]. In addition,

191 the linear attenuation coefficient of xenon hydrate is much higher than that of methane hydrate

192 [66,70], which can significantly enhance adsorption of X-rays and thus improve imaging contrast.

193 Serious risks related to the operations with potentially explosive gas under high pressure can be

194 greatly alleviated, since the stability pressure of xenon hydrate is much lower. In brief, xenon

195 hydrate is a convincing substitute of methane hydrate for experimental study. Moreover, according

196 to the latest in–situ NMR and well logging data achieved during natural gas hydrate drilling program

197 in the Shenhu Area [71], pore space of clayey-silt hydrate reservoir is mainly filled with capillary

198 irreducible water, followed by clay irreducible water, with almost no movable water. Thus, excess-

199 gas method is used here to generate connate water condition in the clayey-silt hydrate reservoir.

200 The experimental setup (see Fig.1) is an integrated test system composed of experimental

201 apparatuses and micro-CT facility. Specific parameters of experimental apparatus were introduced

202 in detail in the previous work [53]. At preparation stage, micro-CT operation is tested. The scanning

203 resolution of sample A (clay-rich) is 5.04μm, while it is 2.54μm for sample B (sand-rich). Then,

204 xenon gas is charged and discharged for several times in the chamber (loading sample) to exhaust

205 the air.
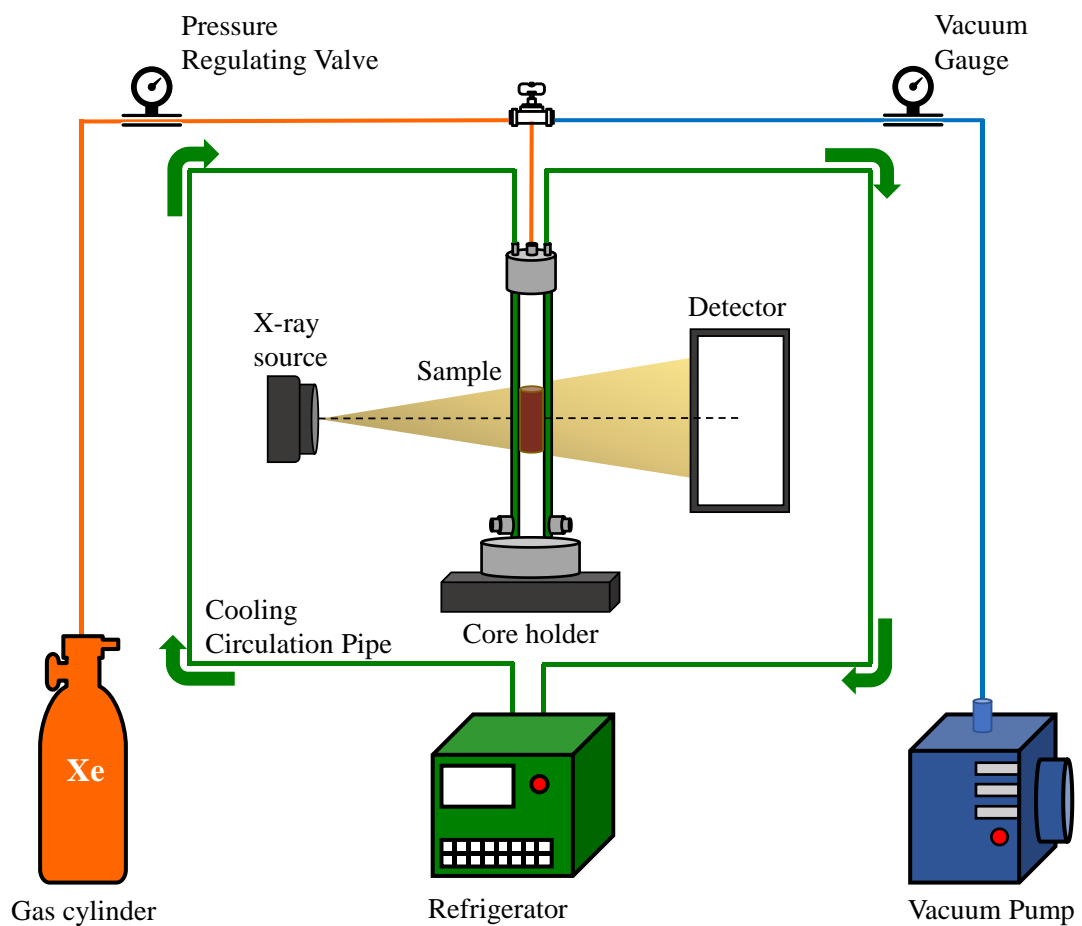


206

207 **Fig. 1 Experimental setup, including micro-CT and experimental system of hydrate phase**
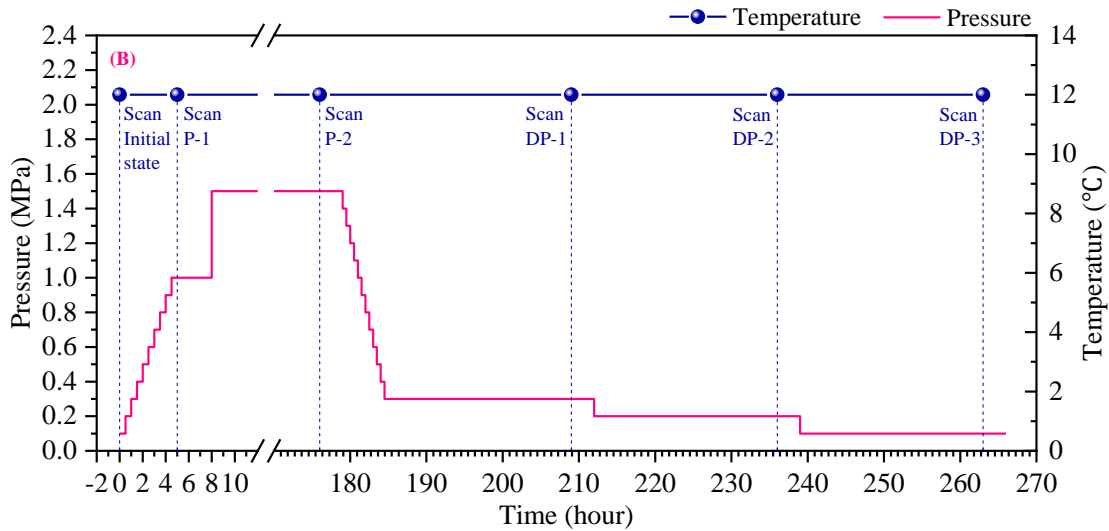
208 **transition**

209 **Experimental procedures.** Fig. 2 depicts pressure-temperature paths over the entire experiment

210 with temporal distribution of micro-CT scans of clayey silts. Temperature is controlled at

211 approximately 285.15K (12°C) throughout the process. Stepwise pressurization method is utilized

212 for hydrate formation and stepwise depressurization is used during decomposition. As shown in

213 previous studies, most of the clayey silt is unconsolidated with a labile structure [72-76]. The

214 microstructure and fluid distribution will be influenced if a larger pressure gradient is applied, and

215 thus a relatively small pressure gradient should be applied to avoid potential damage. Preliminary

216 tests for hydrate formation and decomposition with different pressure gradients were carried out.

217 Based on the results of a series of preliminary tests, the pressure gradient for hydrate formation,

218 which cannot only greatly maintain the original porous space, but also control the formation process

219 within an appropriate period. Moreover, small gradients were also used to capture the initial pressure

220 of hydrate phase transition for analyzing the hysteresis phenomenon (Section 3.4).

221 Multiple CT scans are conducted within phase transition process. The CT scan of 'Initial State' is

222 obtained before injecting gas into the chamber, and the initial scanning time is set as time '0'. In the

223 stage of pressure-induced hydrate formation, xenon gas is injected continuously into the chamber

224 with initial pressure equals to 0.1 MPa and then the pressure was increased stepwise with an interval

225 of 0.1 MPa until hydrate was formed in the sample. Hydrate formation starts when pressure

226 increased to 1.1MPa in sample A, to 1.0MPa in Sample B; then second CT scan, 'P-1', is performed

227 immediately. Subsequently, xenon gas continues to be injected into the chamber until the pressure

228 reaches 1.5 MPa to ensure sufficient hydrate formation. CT scan 'P-2' was performed after 7 days

229 (168 hours) at this pressure-temperature state to obtain the initial fluid-hydrate-gas-solid distribution

230 before hydrate decomposition. The pressure was then reduced stepwise with an interval of 0.1MPa

231 to study hydrate decomposition process. The first CT scan of hydrate decomposition process, 'DP-

232 1', was conducted 24 hours after initial hydrate decomposition (the pressure at this point of sample

233  A is 0.6 MPa and that of sample B is 0.3 MPa). The pressure continues to drop by 0.1MPa, and CT

234  scan 'DP-2' is performed after keeping at this state for 24 hours. This process is repeated until

235  hydrates disappear thoroughly, and then the pressure is released as the atmosphere pressure.
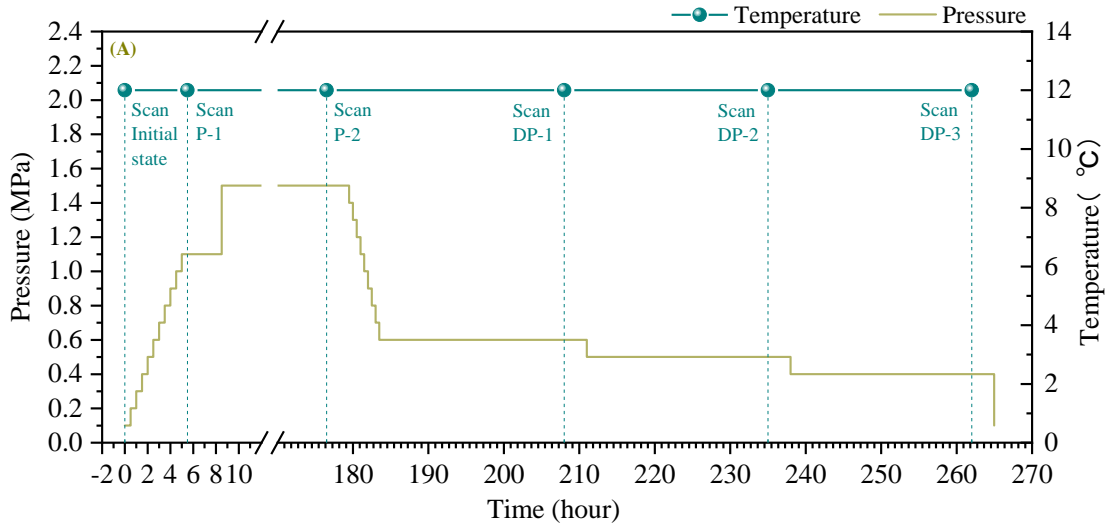
236



237

238

239  **Fig. 2 The pressure-temperature path throughout phase transition experiment and the**

240  **temporal distribution of micro-CT scans for sample (A) and (B) (including Initial State, P**

241  **(Pressuring)-1, P-2, DP (Depressurization)-1, DP-2 and DP-3)**

242  **2.3  Micro-scale characterization and modeling based on images**

243  **Image postprocessing.** Equipment operating conditions (such as current, voltage, etc.) and

244 instability of external conditions (such as temperature and pressure) during imaging process will

245 affect sensors and circuit elements, and therefore generate image noise. In this work, the non-local

246 means filter [77] is utilized for 2D and 3D image denoising while preserving the original information

247 of the image greatly. The watershed algorithm [78] is then applied for phase segmentation based on

248 the atomic number contrast of SEM images (including 2D BSE and 3D FIB-SEM images) or on the

249 relative radiodensity of various materials to X-rays in micro-CT images. Thus, the resulting

250 segmented gray-scale images can be used for further micro-scale characterizations and simulations.

251 **Minerals characterization**. Through enlarging 2D MAPs images, different types of mineral grains

252 and pore space structures at whatever positions can be clearly observed. Based on Qemscan images,

253 minerals content of samples can be quantitatively analyzed. Therefore, not only mineralogical

254 information, but also grain morphology, mineral embedded characteristics and elemental

255 occurrences of the clayey silt samples can be obtained.

256 **Particle size distribution.** Minerals can be separately extracted and marked based on 2D MAPS

257 images with high resolution. The single particle size can be calculated with the method of equivalent

258 diameter, as shown in Eq (1),

$$E_q D = \sqrt{\frac{4*S_{area}}{\pi}}$$ (1)

260 Where $E_q D$ denotes equivalent circular diameter, $S_{area}$ denotes the surface area of the single particle.

261 Finally, the particle size distribution can be statistically summarized.

262 **Pore space characterization.** Pore space characterization based on 2D MAPS images is to acquire

263 the equivalent aperture of pores through central axis method, after which the continuous distribution

264 of multi-scale pore size can be obtained by statistical analysis.

265 While based on 3D images, porosity of clayey silt samples can be calculated as the fraction of pore

266 voxels over the total voxels. Pore size distributions are obtained by NMR simulations. NMR

267 relaxations are simulated using the Random Walker algorithm [79,80]. Throat size distributions are

268 obtained by performing mercury injection simulations in 3D digital models. Moreover, tortuosity of

269 the pore space can be obtained by simulating Brownian Motion of diffusive particles (random

270 walkers) through pore space using the Random Walker Method [81]. These methods have been

271 described in detail in previous study [53] and will not be repeated here.

272 **Intrinsic permeability simulation.** In this study, computational fluid dynamics (CFD) simulations

273 are performed in 3D digital models to obtain absolute permeability in one certain direction. The

274 fluid flow in porous space is assumed to be extremely slow and incompressible. The linear Stokes

275 Equations are solved by the finite difference method (FDM). Specific introduction was described in

276 detail in previous work [53].

277 **3. Results and discussions**

278 **3.1 Fundamental characteristics of clayey silts**

279 Fig. 3 shows the backscattering SEM images of sample A and sample B with magnifying parts

280 indicating dominant minerals and various types of pore space. The Fig. indicates that particles in

281 both samples are randomly arranged and unconsolidated. Particle size of sample A is much finer

282 than that of sample B. In sample A, the proportions of carbonate (basically in the form of biological

283 fossils) and clay are relatively high. Other minerals (such as quartz, mica and feldspar, etc.) are

284 almost tightly surrounded by clay minerals. The porous space in sample A can be classified as

285 microfractures, biological fossil pores (mainly foraminifera), interparticle pores, and clay

286 intercrystalline pores. Among them, biological fossil pores and clay intercrystalline pores comprise

287 a large proportion of total porous space.

288    As for sample B, porous space occurs mainly in the form of large pores, interparticle macropores

289    and clay intercrystalline pores. The proportion of biological fossil pores is much less than that of

290    sample A. Particles are relatively loose-packed. Clay minerals do not totally fill the pore space

291    among large-grained minerals, but mostly surround these minerals.



292

293
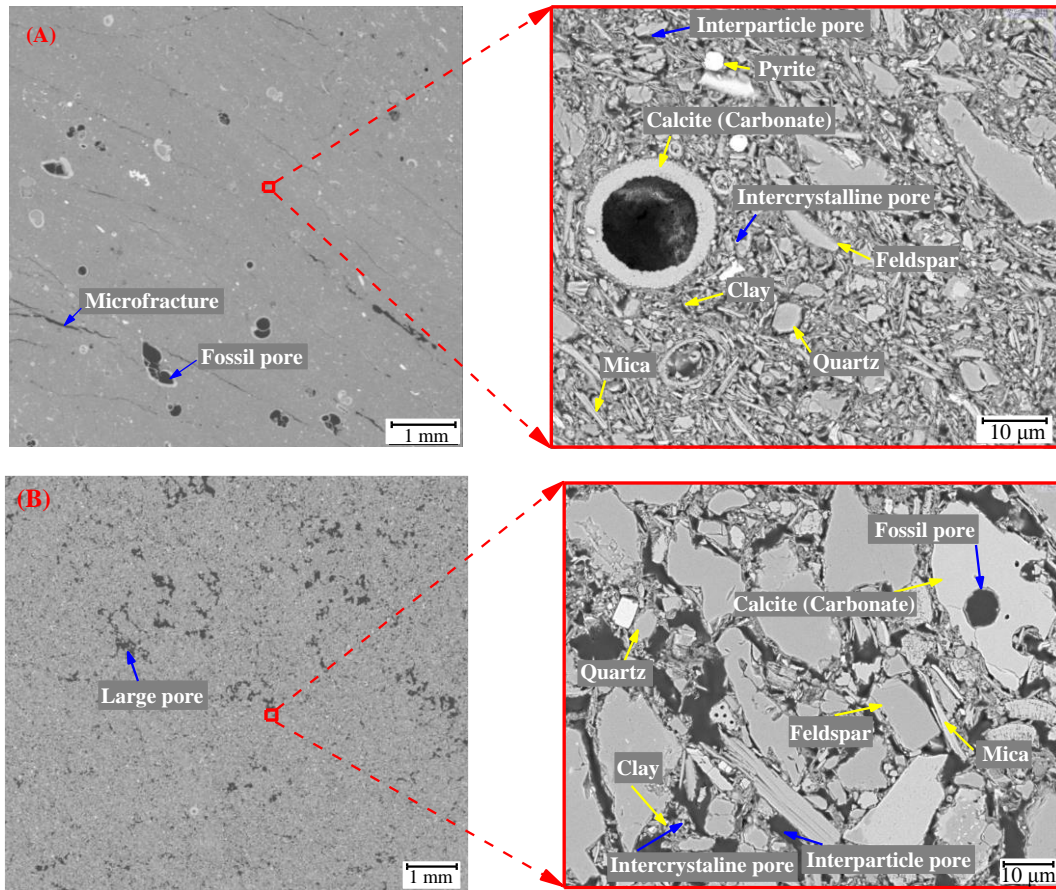
**Fig. 3 MAPS images of Sample (A) and (B) with magnifying parts showing main types of**

**minerals and pore space**

296    **Minerals.** Occurrences of particles with different shapes and dimensions in the two samples suggest

297    complicated compositions and heterogeneous distributions of clayey silt minerals. Fig. 4

298    demonstrates quantitative characterization of minerals in both samples. Moreover, minerals are

299    classified into several main types (including carbonate, clay, quartz, mica, feldspar, pyrite and others)

300    and their proportions are shown in Fig. 4 (C). For sample A, the ratio of carbonate (mainly presenting

301 in biological fossils) is the highest at 37.03%; the second is clay, whose content is more than a

302 quarter of the whole; and quartz accounts for approximately 18%. While for sample B, the most

303 abundant mineral is quartz (44.43%), and both clay and carbonate occupy approximately 16%.



304
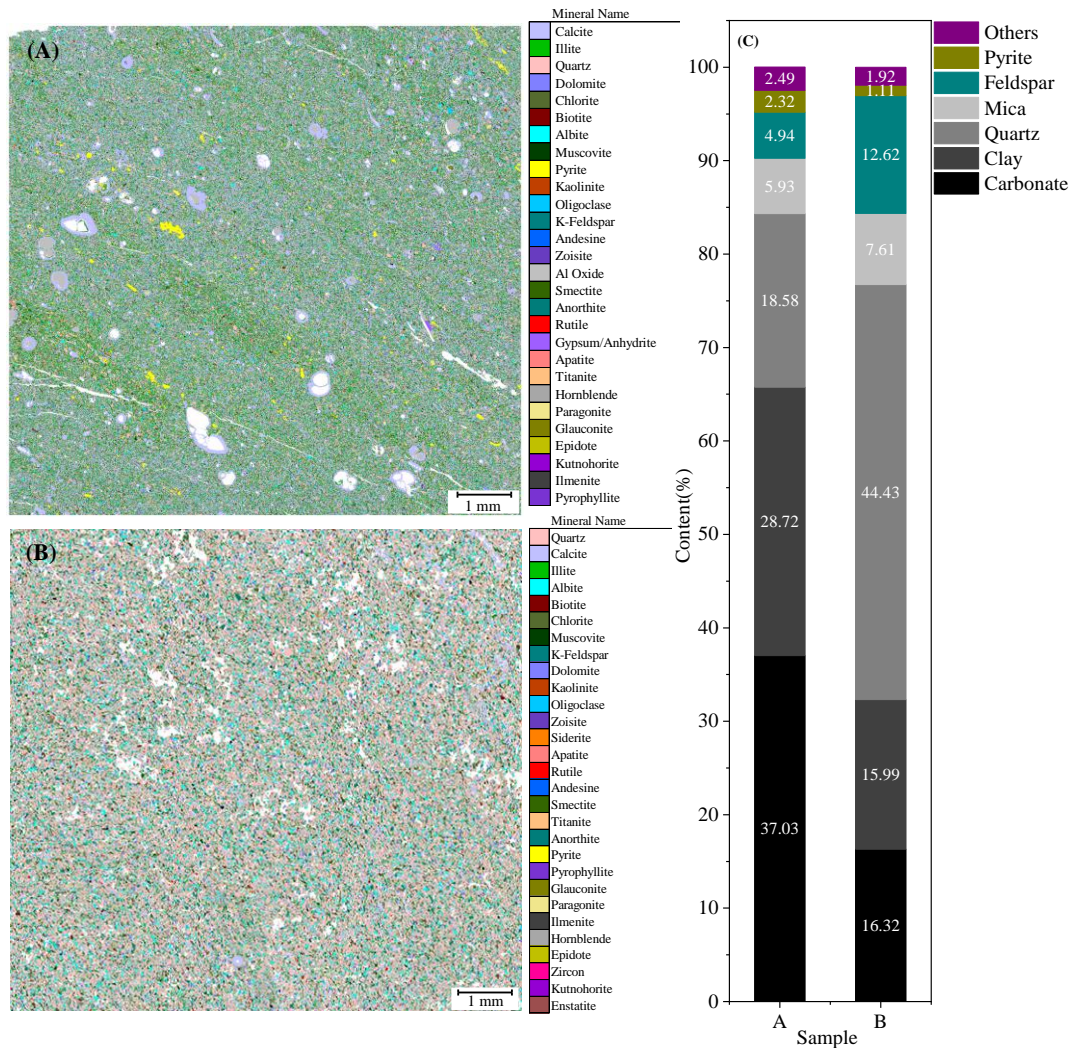
**Fig. 4 (A) Qemscan image of sample A; (B) Qemscan image of sample B; (C) Proportions of**

305

**main mineral categories in the two clayey silts**

306

307 According to Fig. 5, particle size range of sample A is relatively wide. The first peak of the

308 distribution curve (A) occurs at the particle size of approximately 4μm, which is contributed mainly

309 by clay minerals. While the second peak occurs at the particle size of 450μm, representing the

310 abundant biological fossils (such as foraminifera). The distribution curve of sample B peaks when

311　particle size reaches 40μm, which is approximately 10 times larger than that of sample A (excluding

312　biological fossils).
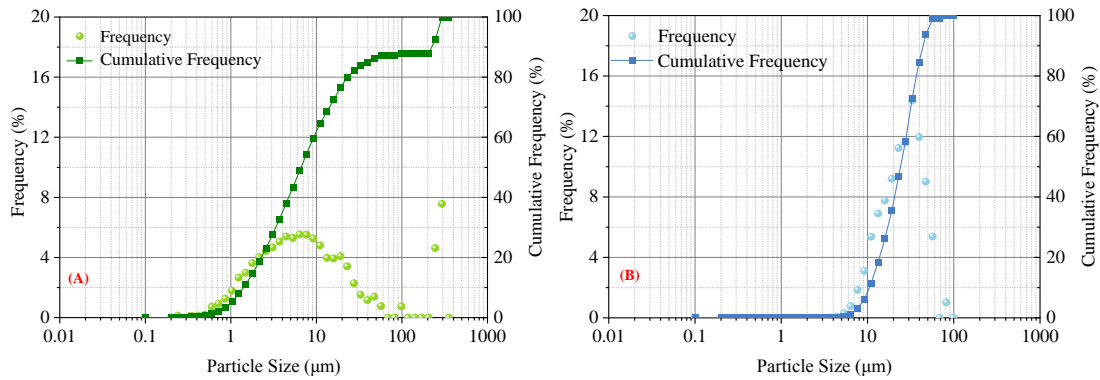


314　**Fig. 5 Particle size distribution of sample (A) and (B) based on MAPS images**

315　**Pore space and seepage capacity.** Firstly, the large-area pore size distributions of samples (Fig. 6)

316　are obtained based on MAPS images. The radii of pores in sample A covers a wide range from

317　submicron to submillimeter. Among them, 83.4% of the pores are submicron-scale pores. The curve

318　peaks at 18.1% when the pore radius is 0.25μm. Submillimeter pores are intragranular pores of

319　biological fossils, accounting for approximately 1%. The distribution curve of pore radius in sample

320　B peaks at 10.1% when the pore radius equals 1μm. There is a low peak (1%) between 0.1μm and

321　0.2μm in pore radius. The number of pores with radius between 1μm and 10μm accounts for 55.4%

322　of the total, and the proportion of submicron pores occupies 32.6%, which denotes that more than

323　half of the pores in sample B are macropores or intergranular pores.
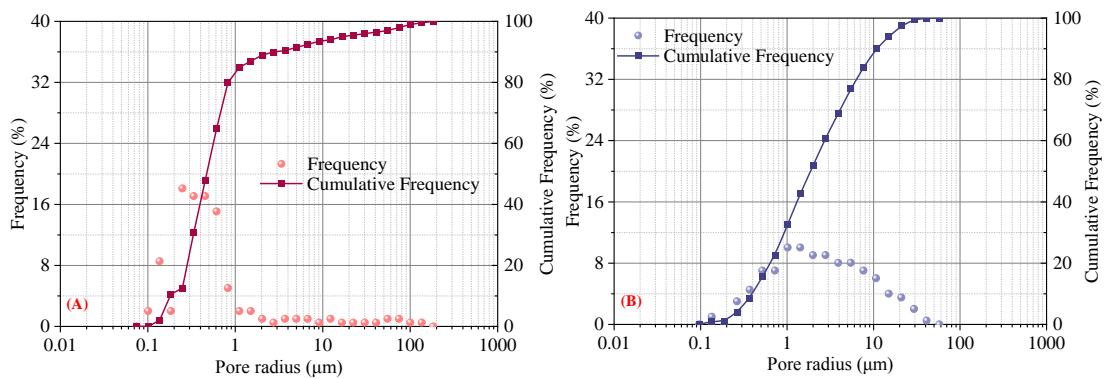


325　**Fig. 6 Pore size distribution curves based on MAPS images of sample (A) and (B)**

326    Larger-sized micron-scale and millimeter-scale pores increase the total porosity of clayey silts and

327    provide potential space for hydrate aggregates. However, plenty of submicron-scale or even

328    nanoscale clay intercrystalline pores in silty matrix is the main factor affecting hydrate formation

329    and seepage characteristics, which cannot be well identified at the resolution of MAPS images.

330    Therefore, FIB-SEM scanning with a resolution of 65nm and micro-CT scanning with a resolution

331    of 0.95μm are conducted respectively on silty matrix of sample A and B. Previous research shows

332    that the selection of typical REV can promote analysis efficiency (accuracy) [82-84]. Fig.7 shows

333    the respective REV model of silty matrix of the two samples. Relative threshold segmentation

334    process and gray distribution curves have been shown in Appendix B. Through size independence

335    verification (detailed in Appendix C), the side length of the REV from clay-rich clayey silt matrix

336    is determined to be 300 pixels, while that of the REV from quartz-rich clayey silt matrix is 500

337    pixels. Simulated physical parameters of pore space and seepage capacity of two sample matrix are

338    listed in Table 1. Pore-throat size distribution curves are depicted in Fig. 8.
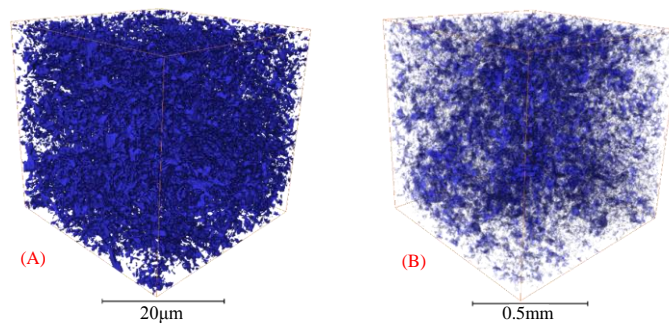
339



340    **Fig. 7 The respective REV model of silty matrix in sample (A) and (B)**

341    **Table 1 Porous space and seepage characteristics of the matrix part in clayey silt samples**

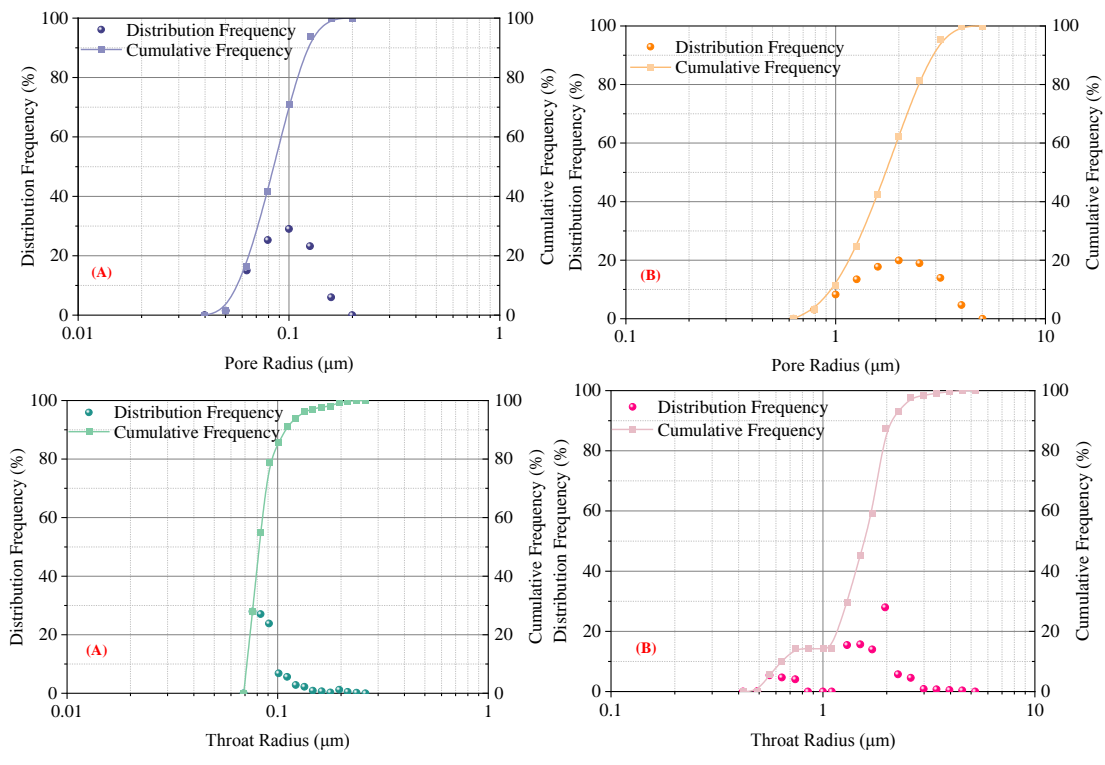| Sample | Porosity [%] | Effective Porosity [%] | Permeability [md] | Tortuosity | Mean Pore Radius [μm] | Mean Throat Radius [μm] |
|--------|--------------|------------------------|-------------------|------------|------------------------|--------------------------|
| A | 16.46 | 15.78 | 0.0126 | 13.55 | 0.0998 | 0.0917 |
| B | 19.67 | 18.98 | 8.68 | 9.1 | 2.06 | 1.38 |

**Fig. 8 Pore-throat size distributions of silty matrix in sample (A) and (B) based on 3D pore**

**space models**

Table 1 demonstrates that porosity values of the silty matrix in the two samples are similar. The

effective porosity accounts for more than 95% of the respective total porosity, indicating that pores

in the two silty matrixes are well-connected. However, due to the high content of fine-grained

minerals (mainly clay minerals) in sample A, the mean pore radius and mean throat radius are both

less than 0.1μm, which are less than one tenth of those in sample B. Combined with Table 2 [85], it

can be seen from Fig. 8 that more than 70% of pores and 85% of throats in sample A matrix are

categorized as microcapillary interstice. While nearly 90% of pores and more than 85% of throats

in sample B matrix are classified as capillary interstice.

**Table 2 Pore categories, respective size range and flow characteristics [85] (Φ denotes pore**

**diameter, f_w denotes fracture width)**

| Pore categories | Size range [μm] | Flow Characteristics |
|---|---|---|
| Supercapillary | Φ > 500 or | Fluids can flow freely under gravity with a high flow rate or even a |

| | | |
|---|---|---|
| interstice | $f_w > 250$ | vortex. |
| Capillary interstice | $0.2 < \Phi < 500$ or $0.1 < f_w < 250$ | Fluids cannot flow freely due to the capillary force. Liquids can flow inside the pores only if the external force is greater than the capillary resistance. |
| Microcapillary interstice | $\Phi < 0.2$ or $f_w < 0.1$ | The attractive force between the fluid and the surrounding medium molecules is always extremely large, and an ultra-high pressure gradient is required for fluids migration. |

356    Moreover, tortuosity of the pore space inside silty matrix of sample A is higher and the fluid flow

357    should be more complicated. Simulation results confirm that although porosity values of the two

358    samples are similar, their seepage capacities differ significantly. According to Chen et al. [86], silty

359    matrix of sample A with the permeability of far less than 0.1md belongs to tight reservoir. While

360    permeability of that in sample B is more than 680 times that in sample A, and sample B matrix

361    belongs to low-permeability reservoir.

**3.2  Hydrate occurrence in clayey silts**

363    Micro-CT images of the clay-rich clayey silt (sample A) at typical states are listed in Fig. 9. Some

364    microfractures are randomly distributed, which makes the structure highly heterogeneous. Three of

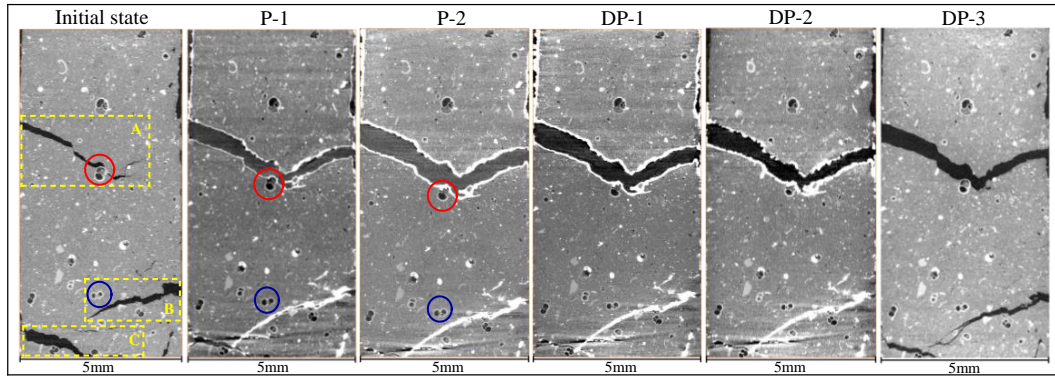365    them are circled with yellow dashed box and denoted as A, B and C, respectively.
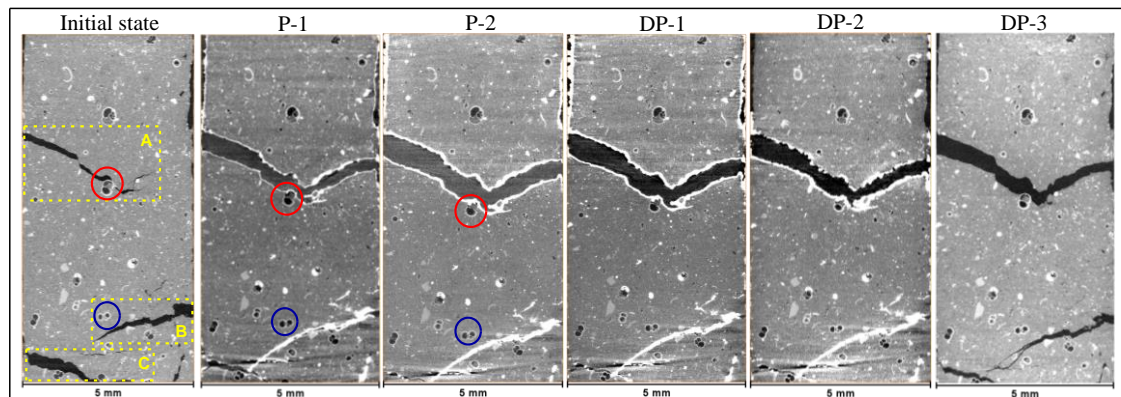


366

**Fig. 9 Micro-CT images of sample A at different states of hydrate phase transition**

**Hydrate formation in clay-rich clayey silt**. At the early stage, the injected gas with the increasing pressure cannot flow into the matrix due to the ultra-low permeability of the dense clay-dominated silty matrix. Thus, xenon gas accumulates in fracture A, which is in good connectivity with the external space. Meanwhile, hydrates form rapidly along fracture sidewall. Since hydrates in fracture A are in direct and sufficient contact with gas, the water in matrix gradually diffuses to the surface of hydrate layer [87] for further hydrate formation. Both the outward migration of internal liquid and the accumulation of injected gas cause local compression of the unconsolidated sediment. As a result, fracture A is transformed into a penetrating fracture with increasing aperture (shown in the state P-1 and P-2), providing more space for hydrates. In this case, hydrates would fill the entire fracture if gas and water could be sufficient.

As for fracture B in a deeper position, the fracture aperture is similar with that of fracture A at initial state. Gas gradually invades forward till fracture B is connected with fracture C. In the meanwhile, a certain amount of hydrate is formed in B and a thin hydrate layer occurs along sidewall of C. However, the upper matrix continuously moves downward, which hinders gas from entering fracture B and impedes subsequent hydrate formation. As a result, hydrate in fracture B only shows a slight increase during later formation and the occurrence of hydrates appears as fracture-filling.

385   While for fracture C, the aperture is the widest at the initial state. However, due to the poor

386   connectivity between fracture C and gas, it narrows once the pressurized gas is injected into the

387   sample. It is not until the limited gas in fracture B breaks into fracture C that a thin hydrate layer is

388   formed on the sidewall of C. Subsequently, hydrate formation in C is terminated due to gas supply

389   disruption. Fracture C is continuously compressed until the previously formed hydrates fill its space.

390   In addition, it is difficult for gas to enter inside matrix pores due to the ultra-high capillary force

391   caused by both microcapillary interstice and the water film surrounding clay particles. On the other

392   hand, hydrate formation continuously extracts water from the matrix to the previously formed

393   hydrates (microfracture-filling and foraminifera-filling in this study) and the matrix becomes

394   compacted at the meanwhile [88]. Thus, although the direct verification is limited by the resolution

395   of micro-CT, it should be hard to form dispersed pore-filling (embedded) hydrates in such capillary

396   and microcapillary interstice of clay-dominated silty matrix. Hydrate mainly exists in the form of

397   fracture-filling and foraminifera-filling.

398   **Hydrate decomposition in clay-rich clayey silt**. In the initial stage of depressurization (from P-2

399   to DP-1), hydrates in fractures remain unchanged, while those in the gap between the sample and

400   the chamber decrease obviously. From DP-1 to DP-2, the uniformly distributed hydrate layer on top

401   of fracture A decomposes into discontinuous particles, indicating inhomogeneous hydrate

402   decomposition. Meanwhile, the thickness of hydrate layer at the bottom slightly increases, and the

403   volume of hydrate aggregation at the lowest position becomes larger. It is analyzed that the

404   decomposed water of top hydrates in fracture A migrates to the bottom, and then re-form hydrates

405   with the trapped decomposed gas [60] under local high pressure and local reduced temperature.

406   During this period, hydrates in fracture B and C still remain undecomposed. At the final state (DP-

407  3), hydrates in fracture A, B and C completely decomposed; however, the structure of fractures

408  cannot recover to the initial state. Specifically, the apertures of the fractures are narrowed compared

409  with that at the initial state, fracture A remains penetrated and fracture B is prolonged accordingly.

410  The gap between the matrix above fracture A and the chamber wall obviously shrink, which

411  indicates an expansion of the above matrix. It is speculated that the decomposed water absorbed into

412  the matrix by the massive clay minerals leads to this phenomenon. However, specific distribution

413  of decomposed water cannot be identified due to the resolution limitation of the current micro-CT

414  technology.

415  **Hydrate formation in quartz-rich clayey silt**. Fig. 10 shows Micro-CT images of quartz-rich

416  clayey silt (sample B) during hydrate phase transition with amplifying images of two local areas. At

417  the initial state, sample B is loosely packed with intensively-distributed microfractures and pores

418  inside, and no dominant channel exists between the sample and the chamber wall. In the early stage

419  of hydrate formation (P-1), gas invades microfractures and hydrate forms at the meanwhile. From

420  the local amplifying image at P-1, it can be seen that some microfractures (red dashed box) are

421  completely filled with hydrates. Some hydrates displace sediment grains and occur in the form of

422  nodulus. While other hydrate particles are scattered (blue dashed box) in microfractures and

423  gradually connect with each other with the increasing hydrate saturation. As a result, the dispersed

424  spheroid and discoid hydrate particles transform into vein hydrates with a greater aspect ratio. This

425  phenomenon has also been found in the research of Wu et al. [49].

426  The sample is continuously squeezed downward at the same time as gas injection. The pore space

427  where hydrates have not yet formed is compressed till the surrounding particles are tightly packed;

428  while pores and microfractures partially occupied by hydrates are squeezed till the hydrates can

429 support the compressed porous space. This phenomenon is consistent with the previous research

430 that hydrate will act as the skeleton in clayey silt sediment with the increasing hydrate saturation

431 [41,89]. And hydrate formation in fine-grained sediment can increase the strength of sediment to

432 some extent. Top surface of the sample gradually becomes concave with pressurization, causing

433 further compression of matrix porous space. The previously formed hydrate deforms to some extent.

434 Besides a few microfractures and pores well-connected with the sample-chamber gap or top gas

435 source, most of the new-generated hydrates from P-1 to P-2 are located in the gap. This phenomenon

436 should be caused by water migration from matrix to the gap during compression. Finally, hydrates

437 in quartz-dominated clayey silt mainly show in microfracture-filling (vein) and grain-displacing

438 (nodulus) forms.



439
440
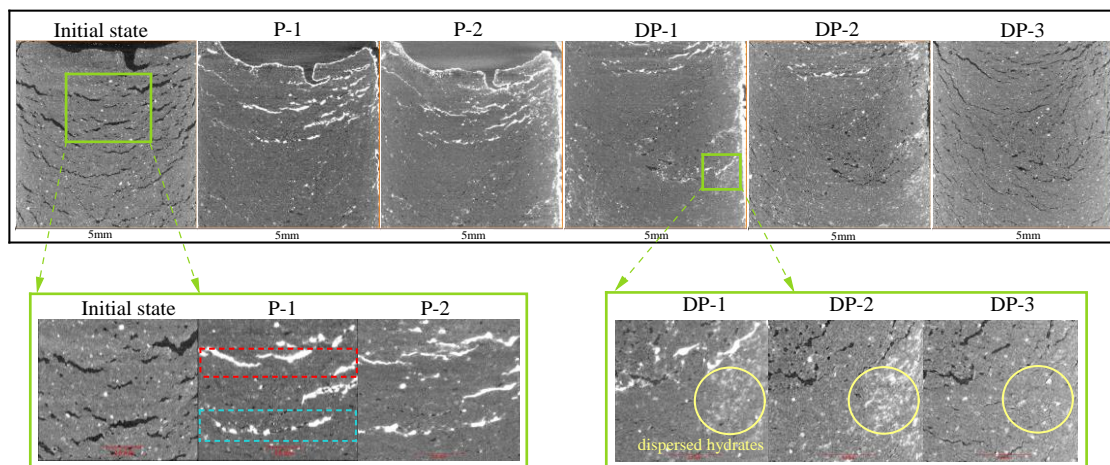
441 **Fig. 10 Micro-CT images of sample B at different states of hydrate phase transition**

442 **Hydrate decomposition in quartz-rich clayey silt.** In the initial stage of depressurization (DP-1),

443 decomposition starts in the chamber-sample gap and the microfractures well-connected to the

444 external porous space. Dispersed hydrates (in yellow circles) that not present during formation occur

445 in matrix at state DP-1. After pressure drops to DP-2 and maintains for 24 hours, the dispersed

446 hydrates do not disappear, but show a significant increase. It is analyzed that hydrates in the pore

447 space well-connected with the outside gradually decompose with pressure decrease, throats

448 connecting with the internal pore space become wider. Therefore, pressure is gradually transmitted

449 to the interior of matrix, causing further hydrate decomposition. During this period, the support

450 cementation is significantly lost with decreasing hydrate saturation, which leads to the decrease of

451 hardness and failure strength of clayey silt sediment [90]. The matrix gradually migrates downwards.

452 Meanwhile, hydrates in the chamber-sample gap decompose and the sample laterally extends until

453 it is in close contact with the chamber wall. As a result, the well-connected pore space and the

454 dominant migration channels (chamber-sample gap) for decomposed gas and water disappear. As

455 the matrix pores in sample B belong to the category of capillary interstice, molecular gravitational

456 forces are always exerted between the liquid particles and between the liquid and the pore walls.

457 High capillary force prevents internal fluids from flowing freely. The local temperature decrease

458 caused by hydrate decomposition and the local pressure increase caused by the accumulation of

459 decomposed gas and water lead to hydrate reformation. The reformed hydrates appear in dispersed

460 pore-filling habits embedded in the silty matrix. The embedded type of hydrate occurrence has also

461 been found in the research of Wu et al. [49] and Dai et al [41]. Pressure drops further to DP-2,

462 fracture-filling hydrates continuously decompose. The decomposed gas and water flow into matrix

463 pores, and are still trapped under molecular gravitational force. And the conduction of external

464 pressure drop is still hindered by high capillary force. Thus, more dispersed pore-filling hydrates

465 occur due to local temperature decrease and pressure increase. At the final stage of depressurization,

466 matrix gradually becomes loosely packed and hydrates decompose completely. Abundant

467 microfractures and matrix pores reappear. However, the inside structure is significantly different

468    from that at the initial state.

469    In conclusion, for clay-dominated clayey silt reservoir, fine matrix particles are densely packed.

470    Under the ultra-high capillary force and the strong adsorption force of clay minerals on water, it is

471    difficult for gas to enter the microcapillary interstice in matrix. In general, gas can invade forward

472    through microfractures and the formed hydrates are in the shape of fracture-filling. As for the initial

473    fractures with large aperture or the penetrating fractures, hydrates grow in layer on fracture sidewalls

474    and are gradually thickened. Hydrates would fill the fracture if gas and water could be sufficient.

475    For both cases, hydrates continuously squeeze the surrounding matrix and widen fractures during

476    growth, leading to the damage of porous space where no hydrate formed initially. Hydrates mainly

477    exist in the form of microfracture-filling (vein) and foraminifera-filling. While the quartz-dominated

478    clayey silt reservoir is rich in microfractures and matrix pores. Due to the high content of pores

479    above submicron level, the connectivity between internal porous space and gas is better. Hydrates

480    are in the form of grain-displacing (nodulus) and microfracture-filling (vein).

481    During hydrate decomposition, clay-dominated clayey silt migrates downward under gravity due to

482    the loss of support from hydrates. Consequently, sediment strength decreases, fractures are narrowed.

483    Finally, matrix structure is significantly different from that at initial state. Likewise, hydrates

484    dissociation in quartz-dominated clayey silt starts from the locations that is well-connected with the

485    external porous space. During decomposition, the disappearance of dominant channels

486    (microfractures) as well as the accumulation of decomposed water and gas can lead to an increase

487    of pore pressure and a decrease in temperature, which can cause re-formation of dispersed hydrates

488    in matrix pores. There still be a large amount of microfractures and matrix pores after complete

489    hydrate decomposition. However, the aperture of most fractures is narrowed and the matrix structure

490 differs from that at initial state.

491 The results possess theoretical importance for practical development of clayey silt hydrate reservoirs.

492 Targeted reconstruction methods should be implemented for reservoirs with different mineral

493 compositions and hydrate occurrences. Appropriate reconstruction can largely ensure productivity

494 by reducing the transformation from fracture-filling to dispersed pore-filling (embedded) hydrate

495 and thus the discontinuity of production in quartz-rich reservoirs, or alleviating the shrinkage or

496 even disappearance of dominant channels for decomposed gas and water in clay-rich reservoir.

497 Moreover, for achieving long-term development of clayey silt hydrates, thermal stimulation should

498 be taken as a parallel measure to weaken hydrate re-formation and its adverse impacts.

499 **Error analysis between in-situ reservoir conditions and laboratory conditions.** The results

500 shown in this section are based on xenon hydrate phase transition tests at pore scale in laboratory.

501 Due to the better stability of xenon hydrate at lower pressure, the experiment pressure is much lower

502 than the actual reservoir pressure (13.5MPa) [91].

503 For the microstructure of clayey silt sediment, Wu et al. [49] indicate that the void ratio of clayey

504 silt sediment can significantly decrease with the increase of formation pressure. The actual higher

505 pore pressure can enhance cementing bonds, the ability to resist deformation [92], and also increase

506 the elastic modulus for the pore fluid. Therefore, the failure strength of hydrate-bearing sediment is

507 higher, and the failure volumetric strain is lower at the actual reservoir condition. As for hydrate

508 microstructure, Lee et al. [93] demonstrate that the geometry of grain-displacing hydrate formed by

509 filling pore-existing fractures are mostly governed by the geometry of fracture, whereas those

510 formed by heaving mechanisms are governed by in-situ stress conditions and geomechanical

511 properties. Assuming an unlimited amount of methane and an unlimited time for hydrate formation,

the overburden pressure is the key factor for controlling the thickness of hydrate. There is a negative

relation between the thickness of hydrate and the overburden stress [94,95]. Thus, the actual hydrate

thickness should be theoretically smaller than that of hydrates formed in laboratory.

**3.3 Hydrate in foraminifera**

Fig. 11 shows 3D distribution of foraminifera in sample A. The enrichment of foraminifera highly

increases the volume of intragranular pores. According to the previous research, the high abundance

of foraminifera in clayey silt is favorable for the storage and enrichment of hydrates [96,97]. Fig.

12 illustrates that the hard shell of foraminifera can keep their internal space from being compressed

when unconsolidated clayey silt is deformed during hydrate formation. Some foraminifera (e.g., in

the red circle in Fig. 9) are well-connected with external gas source; therefore, hydrates can be easily

generated inside them. As for other foraminifera (e.g., in the blue circle in Fig. 9), clay minerals

tightly wrap their outer shells due to sample deformation during pressurization. The blockage of gas

channels connecting with their inner space prevents hydrate formation in these foraminifera.

Therefore, whether hydrate can form inside foraminifera depends not only on their structure [98],

but also on the types of minerals and matrix structure around them.
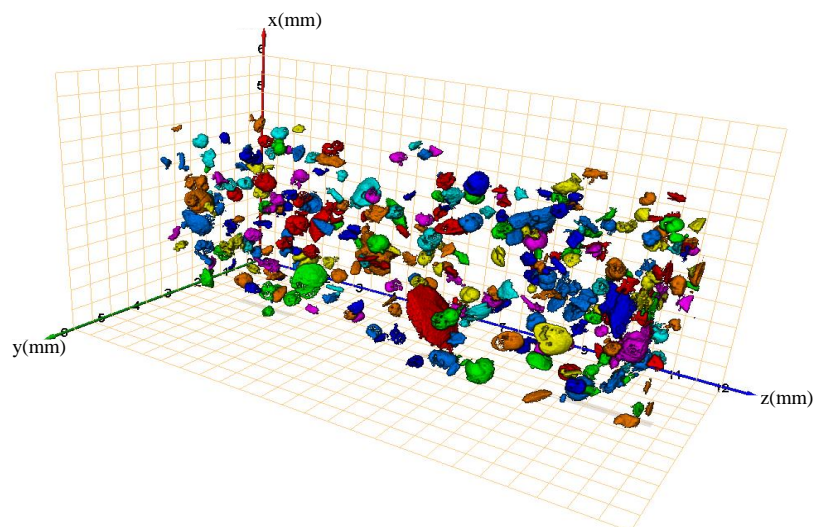


**Fig. 11 3D distributions of foraminifera containing in clayey silt sample A**
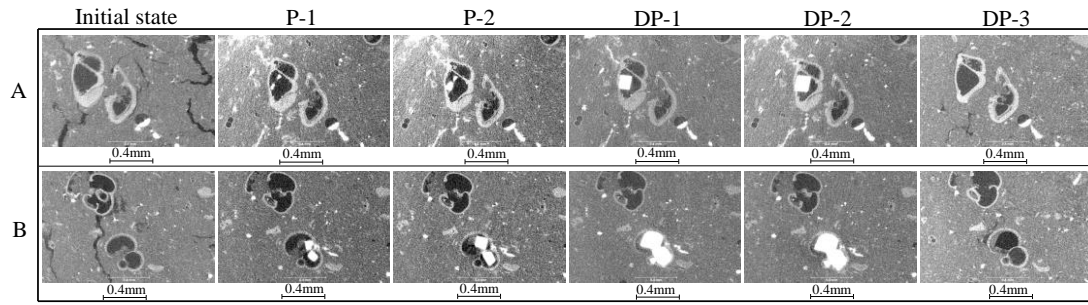
**Fig. 12 Hydrate phase transition in foraminifera in sample A**

531  Two representative examples of hydrate phase transition inside foraminifera are listed in Fig. 12.

532  Two pieces of hydrates in foraminifer A show as pore-filling morphology initially. Then, significant

533  phenomenon of hydrate Ostwald Ripening [99], which is generated by Gibbs-Thomson effect, is

534  observed during process from P-1 to DP-1. That is, two pieces of hydrates merge together and

535  gradually grow into a shape of regular cube. It should be noted that hydrate is only generated in the

536  leftmost foraminifer. The highlighted material in the lower right circular pore should be pyrite

537  aggregates. Likewise, there are two pieces of hydrates generated in foraminifer B. However,

538  Ostwald Ripening phenomenon has not been observed as the two chambers in the shell are separated.

539  Two pieces of hydrates grow as regular cubes in respective space before being confined by fossil

540  walls. Foraminifera-filling hydrate tends to adhere to the inner walls of the shell. If time and/or gas

541  and water source was sufficient, hydrates would fill the entire cavity. Moreover, this type of hydrate

542  is completely surrounded by foraminifera shells, which cannot facilitate the cementation of clayey

543  silt matrix during formation.

544  In addition, hydrate volume in both foraminifera A and B did not reach the highest point at pressure

545  peak (P-2). During depressurization stage from P-2 to DP-2, hydrates inside foraminifera still

546  continue to increase even though partial hydrates in matrix have already decomposed. In summary,

547  foraminifera-filling hydrates in clayey silt reservoir show more significant decomposition hysteresis.

548 **3.4 Hydrate phase transition hysteresis**

549 During hydrate phase transition, the initial formation pressure (P-1) is found to be inconsistent with

550 the initial decomposition pressure (DP-1) at the same temperature. As shown in Fig. 13, the pressure

551 of P-1 of sample A is 1.1MPa, while the pressure at DP-1 is 0.6MPa. As for sample B, P-1 is 1.0MPa

552 and DP-1 is 0.3MPa. In other words, hydrate shows the phenomenon of 'difficult to synthesize,

553 difficult to decompose' in clayey silt. In Fig. 12, the hydrate initial formation (P-1), initial

554 decomposition (DP-1) and final decomposition (DP-3) state points in both samples are projected on

555 the xenon hydrate phase diagram, which is acquired in pure Xe system [100].
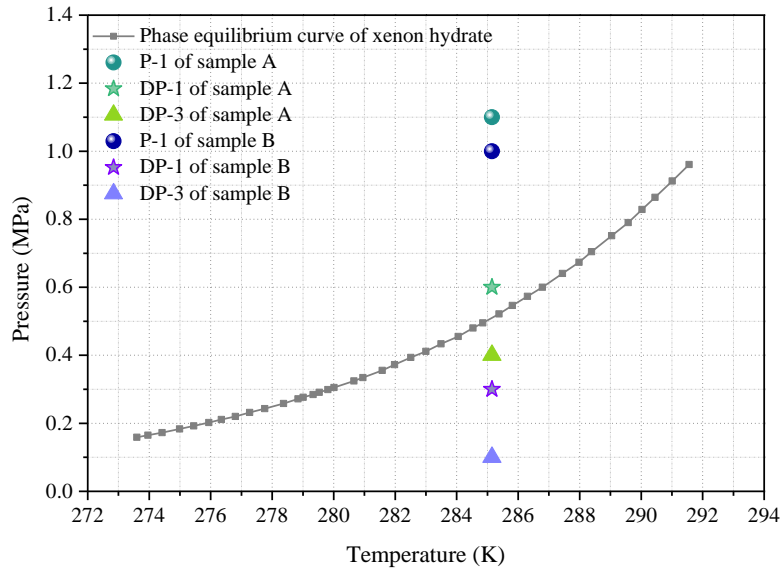
556

557
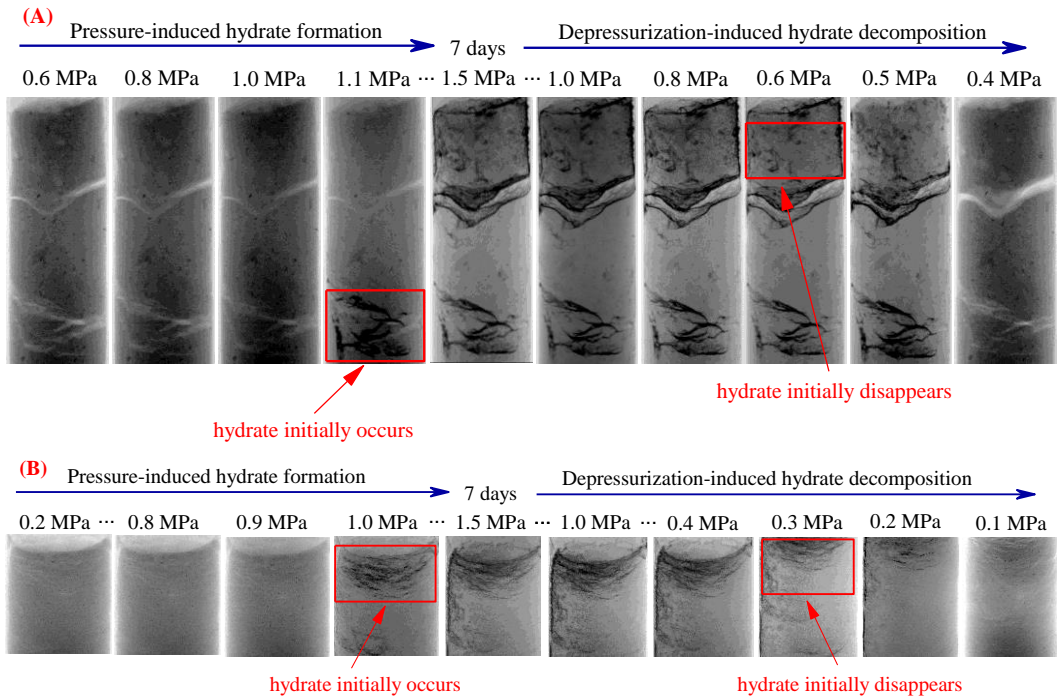
558 **Fig. 13 Micro-CT projections during hydrate phase transition in sample (A) and (B)**

**Fig. 14 Phase diagram of xenon hydrate [100] and the initial formation pressure (P-1), initial**

**decomposition pressure (DP-1) and final decomposition pressure (DP-3) of the two clayey silt**

**samples**

**Hydrate formation hysteresis.** Fig. 14 shows that initial formation pressures in two samples are

different, but both of them are much higher than the equilibrium pressure at the same temperature.

This phenomenon is supposed to be a composite effect of hydrate nucleation condition and phase

boundary shift.

Firstly, when it comes to the hydrate nucleation conditions, Sloan indicated that both the gas phase

and the water phase are disordered at the molecular level, whereas hydrate crystals are intrinsically

ordered [3]. As entropy favors disorder over order, the initial hydrate formation is hindered by a

long, metastable period (induction period). During this period, overpressure (or supercooling) as a

driving force is indispensable for rearranging the disorderly gas and liquid water into the orderly

hydrate crystal structure till the critical size for spontaneous growth. As shown in Fig. 15, hydrate

nucleation and growth have direct analogies in crystallization processes such as the precipitation of

salt from solution [3]. Mullin [101] demonstrated that (1) the right side of the equilibrium line AB

575    is the stable region, in which crystallization is impossible; (2) the area between AB and CD is the

576    metastable (supersaturated) region, in which spontaneous crystallization cannot occur, but if any

577    seed exists in the metastable solution, the seed will grow; (3) the left side of CD is the unstable

578    region, in which spontaneous crystallization can take place. A direct analogy is shown in Fig. 15 (b)

579    for hydrates when the concentration axis of Fig. 15 (a) is replaced by a logarithmic pressure axis [3].

580    The AB and CD lines in Fig. 15 (b) possess the same meaning as in (a) by analogy. To the left of

581    line CD in (b), hydrate nucleation will readily occur due to the high driving force [3]. In summary,

582    a high driving force (overpressure in this study) is required for initial spontaneous hydrate formation

583    in a system without hydrate seeds.



584
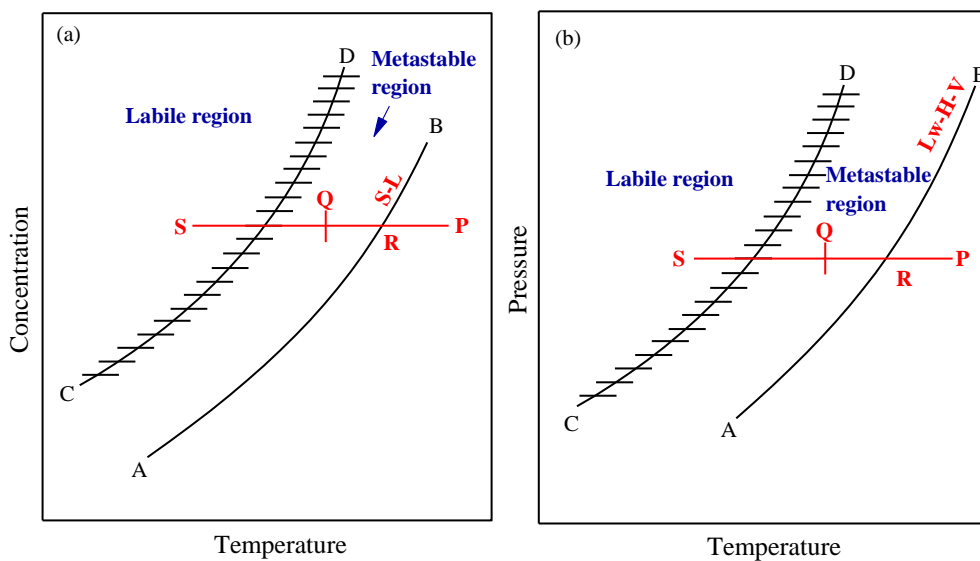
585    **Fig. 15 (a) Crystal and (b) hydrate formation as a function of subcooling relative to the**

586    **equilibrium line (AB) and the spinodal line (CD; supersaturation limit)** [3]**.**

587    Secondly, various factors of practical clayey silt hydrate reservoirs can lead to phase boundary shift.

588    Capillary effect of small pores can shift thermodynamic phase boundary toward lower temperature

589    (or higher pressure), which is referred to as the Gibbs-Thomson effect [102]. Specifically, Liu et al.

590    [103] proposed that capillary effect of pores in fine-grained quartz sand (particle size < 35 μm) is

591 so significant that temperature can be reduced by 0.5-1.5K at the same pressure. Clennell [104]

592 indicated that fine-grained sediments inhibit hydrate formation until the temperature is 0.5-3□

593 below the equilibrium value. Clennell [104] also pointed out that strong adsorption of water by clay-

594 rich sediments can reduce water activity and thus inhibit hydrate formation, especially at high gas

595 saturation. Moreover, Yang et al. [105] demonstrated that saline ions in aqueous solution possess

596 ionic effect, which can destroy ionization equilibrium, alter the equilibrium constant of hydrated

597 ions and thus shift the phase boundary to lower temperature and higher pressure. In summary,

598 hydrate nucleation conditions and phase boundary shift caused by various factors make the initial

599 hydrate formation pressure significantly higher than the equilibrium value.

600 Furthermore, the initial hydrate formation pressure (P-1) in sample A is higher than that in sample

601 B. According to the information in Table 2, an ultra-high pressure gradient is required for gas

602 entering the microcapillary interstices in sample A matrix. Moreover, it is difficult for water to flow

603 freely as the rich clay possesses strong adsorption to water. Therefore, hydrate formation can only

604 start when gas and water are in contact with each other through a high driving force (overpressure)

605 and a slow diffusion process. While for sample B, microfractures are intensively distributed and

606 sizes of matrix pores are larger. Low content of clay minerals possesses weaker adsorption to water

607 and smaller pressure gradient is required for fluid flow in porous space. That is, the driving force

608 required for initial hydrate formation in sample B is lower than in sample A.

609 **Hydrate decomposition hysteresis.** Hydrate decomposition should be easier and faster than

610 hydrate nucleation, as hydrate decomposition is an entropy-increasing process. That is, ordered

611 hydrate crystals develop into disordered gas and water. According to Sloan [3], the theoretical P-T

612 point at which hydrates completely decompose should be infinitely approaching phase boundary.

613 However, both the DP-3 points in Fig. 14 are beneath the phase equilibrium line. In particular, the

614 initial decomposition pressure (DP-1) of the hydrate in sample B is located in the stable region, that

615 is, hydrates have not start to decompose until the system pressure drops to the stable region. It seems

616 to be contradictory with the upper shift of phase boundary during hydrate formation. In some

617 literatures, this unexpected high stability of hydrate at conditions out of thermodynamic equilibrium

618 is also called 'self-preservation' effect [106,107].

619 According to the results in section 3.1, matrix pores of sample B are mostly capillary interstices,

620 and hydrates mainly occur as grain-displacing (nodulus) and microfracture-filling (vein) types.

621 Hydrate formation and creep deformation of clayey silt can lead to a dramatical reduction in porous

622 space. The ultra-high capillary force of narrow throats hinders pressure conduction into pores.

623 Moreover, the pore space of in-situ clay-silt hydrate reservoir is mainly filled by capillary-bound

624 water, followed by clay-bound water, with almost no movable water [71]. Therefore, hydrates

625 remain unchanged until the system pressure drops to a point where the internal and external pressure

626 difference can overcome high capillary force of matrix pores and water adhesion force by clay

627 minerals. While for sample A, hydrates occur as fracture-filling type (except those in foraminifera).

628 The conduction of system pressure is not limited by capillary force. Decomposed water and gas can

629 transport without the hinderance of matrix pores. Thus, initial hydrate decomposition pressure (DP-

630 1) in sample A is higher than that in sample B, that is, hydrate in sample A is easier to decompose.

631 As shown in Fig. 12, foraminifera-filling hydrate is the other main type of hydrate occurrence in

632 sample A. In the early stage of depressurization, clay minerals wrapped around foraminifera restrict

633 pressure conduction. While in later stage, clay minerals hindered the output of decomposed water

634 and gas. According to the results in section 3.3, foraminifera-filling hydrates show a significant

635    decomposition hysteresis. Therefore, the final decomposition pressure (DP-3) of hydrate in sample

636    A is below the phase boundary. For sample B, the thin throats hinder transport of decomposed gas

637    and water, which inhibits further hydrate decomposition. Subsequently, the low temperature caused

638    by decomposition and the high pressure caused by accumulation of gas and water result in hydrate

639    re-formation in pores with smaller size. Thus, the system pressure required for complete hydrate

640    decomposition in sample B is lower than that in sample A.

641    Different hydrate occurrences and mineral compositions of reservoirs can lead to different hysteresis

642    degrees of hydrate phase transition. Targeted depressurization schemes should be adopted for

643    hydrate reservoirs under different conditions. Reasonable pressure depletion together with

644    monitoring system can largely avoid geological hazards potentially triggered by strength reduction

645    during decomposition. The factors and relevant sensitivity analysis of hydrate decomposition

646    hysteresis in reservoirs with inhomogeneous pore distribution and large differences in mineral

647    contents need to be investigated in detail in the future.

648    **4.    Conclusions**

649    In this work, hydrate phase transition experiments are performed in two clayey silts collected at

650    different locations of hydrate reservoir in the South China Sea. The basic characteristics, including

651    mineral compositions and porous space, are qualitatively and quantitatively analyzed. The main

652    conclusions are as follows.

653    1.    In clay-rich clayey silt, more than 70% of the matrix pores (except biological fossils) are

654          microcapillary interstice. And the matrix is classified as tight reservoir (k≈0.01mD). For

655          quartz-rich clayey silt, more than 90% of the matrix pores are capillary interstice and the matrix

656          is low permeable (k< 10mD).

657    2.    For clay-rich clayey silt, hydrates occur in the form of microfracture-filling (vein) and

658          foraminifera-filling. While hydrates mainly exist in the form of microfracture-filling (vein) and

659          grain-displacing (nodulus) in quartz-rich clayey silt.

660    3.    Biological fossils (especially foraminifera) are mainly found in clay-rich clayey silt sample.

661          Although the abundant foraminifera can provide favorable porous space for hydrate formation,

662          the through-holes on some foraminifera shells are tightly blocked by clay minerals, which

663          hinders hydrate formation inside.

664    4.    During hydrate formation in clayey silts, the clay minerals, the saline ions, the high content of

665          fine grains (Gibbs-Thomson effect) and the high driving force (overpressure in this study)

666          required for a critical-size hydrate core formation induced by entropy reduction, can all lead to

667          the shift of phase boundary toward low-temperature and high-pressure condition. This

668          phenomenon of hydrate formation hysteresis is more obvious in the clay-rich sample.

669    5.    The impeded pressure conduction can lead to decomposition hysteresis. Pressure difference

670          must continuously increase for initial decomposition until it can overcome the high adhesion

671          of water by clay minerals and the high capillary force of matrix pores and throats. Hydrates in

672          biological fossils present more remarkable decomposition hysteresis.

673    6.    During hydrate decomposition, silty matrix gradually moves downward due to decreasing

674          strength. For clay-rich sample, the dominant channels for decomposed water and gas will be

675          compressed and affect productivity. While in quartz-rich reservoir, capillary interstice hinders

676          migration of decomposed gas and water, resulting in the dispersed formation of secondary

677          hydrate in silty matrix and the consequent discontinuous gas production.

678    Therefore, for clayey silt hydrate reservoirs with different mineral compositions and hydrate

679 occurrences, both the reservoir stability and the decomposition hysteresis should be taken into

680 consideration, and reasonable depressurization scheme should be adopted together with monitoring

681 system. Targeted reconstruction methods should be used to impede the shrinkage or even

682 disappearance of dominant channels and to avoid the secondary pore-filling (embedded) hydrates

683 dispersed in fine capillary interstice. Moreover, in order to achieve long-term stable development of

684 clayey silt hydrate reservoirs, thermal stimulation should be considered as parallel measure. The

685 future work should focus on how the mechanical and fluid flow properties change with hydrate

686 phase transition, which hope to be contributed to improved measures for impelling efficient

687 development in fine-grained hydrate sediments.

688 **Appendix**

689 **A.   SEM sample preparation**

690 Firstly, the original sample was prepared precisely into a specified shape. Then, the prepared sample

691 was dried in the oven for dry imaging. After that, the argon ion polishing instrument is utilized to

692 polish the sample surface. The principle is that the ionized argon gas accelerate to the sample and

693 the surface is polished by ion sputtering through momentum transfer during collision. As a result,

694 the surfaces are smooth and parallel. And the carbon coater is finally used for protecting sample

695 surface and improving the scanning effect of SEM.

696 **B.   Threshold segmentation and gray distribution curves**

697 For efficient analysis, the original 16bit binary images are firstly transformed into 8bit images. Due

698 to the great variety of minerals, the curves of various substances overlap each other. The integral

699 gray value distribution curve of each silty matrix is shown in Fig. A.1 (A) and (B), respectively. The

700 segmentation threshold of the two phases (solid phase and fluid phase) is determined by the

701 watershed algorithm [108] in Avizo software. The segmented CT images are shown in the figures.

702 The blue represents pore space and the yellow represents rock phase. The threshold value of clay-

703 dominated clayey silt matrix is 129, and that of quartz-dominated clayey silt matrix is 69.
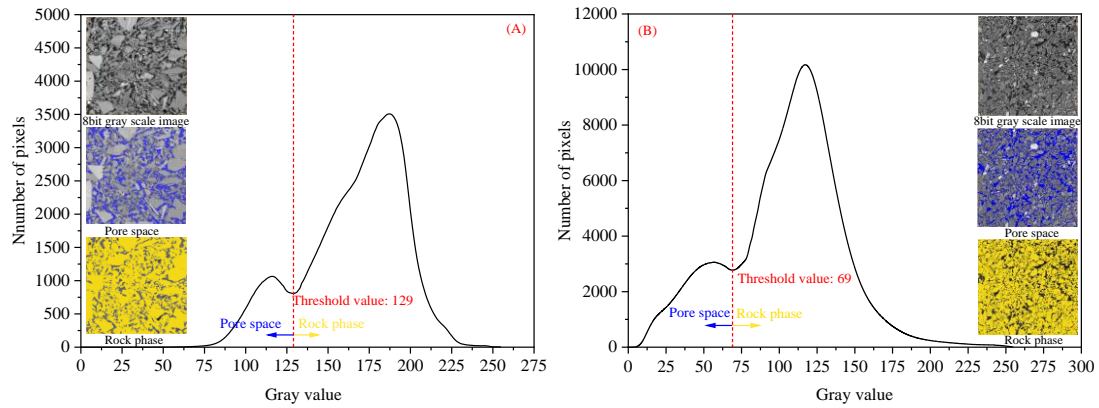
704



705 **Fig. A.1 Gray value distribution corresponding to pore space and rock phase in matrix part**

706 **of the clayey silt sample (A) and (B)**

707 **C.  Size independence verification of the REVs shown in Fig.7**

708 In the silty matrix of the two clayey silt samples, 5 REVs at random positions are selected and the

709 side length of REV (the minimum is 50 pixels) increases with an increment of 50 pixels. The

710 maximum side length of REV in clay-dominated matrix is 500 pixels, while it is 800 pixels in quartz-

711 dominated matrix. The curves of porosity versus side length of REV have been shown in the Fig.

712 A.2 (A) and (B). With the increase of the side length of REV, the porosity gradually converges. The

713 average and the variance of the porosity of REVs with different sizes are calculated. The hypothesis

714 tests (T test and F test) are performed with the values of the maximum REVs, and the confidence

715 interval is 95%. Detailed descriptions of the methods can refer to the research of Liu et al. [109].

716 Finally, the side length of the REV from clay-dominated clayey silt matrix is determined to be 300

717 pixels, while that of the REV from quartz-dominated clayey silt matrix is 500 pixels.
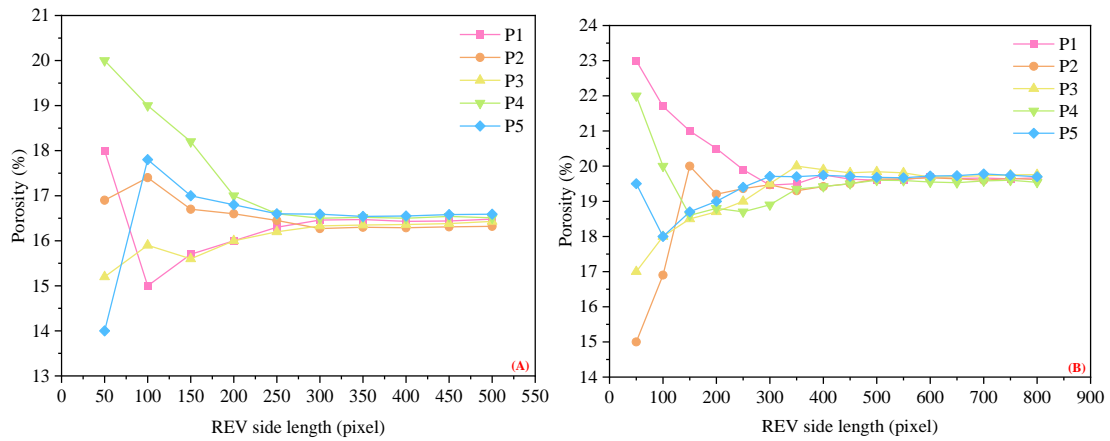
**Fig. A.2 The relationship between porosity and REV side length of the silty matrix of sample**

**(A) and (B)**

**Reference**

[1] Aydin G, Karakurt I, Aydiner K. Analysis and Mitigation Opportunities of Methane Emissions. Energy Sector, Energy Sources, Part A: Recovery, Utilization, and Environmental Effects 2012; 34(11): 967-82, https://doi.org/10.1080/15567031003716725.

[2] Aydin G, Kaya S, Karakurt I. Modeling of coal consumption in Turkey: An application of Trend Analysis. In: 24th International mining congress and exhibition of Turkey-IMCET'15, 14-17 April, Antalya, Turkey; 2015.

[3] Jr S, Koh C. Clathrate hydrates of natural gases. 3rd ed. New York: CRC; 2007.

735    [4]  Moridis GJ, Collett TS, Boswell R, Kurihara M, Reagan MT, Koh C, et al. Toward Production

736        from Gas Hydrates: Current Status, Assessment of Resources, and Simulation-Based

737        Evaluation of Technology and Potential. SPE Reserv Eval Eng 2009; 12: 745-71.

738        https://doi.org/10.2118/114163-PA.

739    [5]  Sloan ED. Natural Gas Hydrate Phase Equilibria and Kinetics: Understanding the State-Of-

740        The-Art. Rev Inst Fr Pét 1990; 45: 245-66. https://doi.org/10.2516/ogst:1990018.

741    [6]  Kou X, Li XS, Wang Y, Zhang Y, Chen ZY. Distribution and reformation characteristics of gas

742        hydrate during hydrate dissociation by thermal stimulation and depressurization methods. Appl

743        Energ 2020; 277: 115575. https://doi.org/10.1016/j.apenergy.2020.115575.

744    [7] Johnson AH. Global resource potential of gas hydrate-a new calculation. In: Proceedings of the

745        7th International Conference on Gas Hydrates (ICGH 2011), Edinburgh, Scotland, United

746        Kingdom, July 17-21, 2011.

747    [8] Qin XW, Liang QY, Ye JL, Yang L, Qiu HJ, Xie WW, et al. The response of temperature and

748        pressure of hydrate reservoirs in the first gas hydrate production test in South China Sea. Appl

749        Energ 2020; 278: 115649. https://doi.org/10.1016/j.apenergy.2020.115649.

750    [9] Ryu BJ, Collett TS, Riedel M, Kim GY, Chun JH, Banhk JJ, et al. Scientific results of the Second

751        Gas Hydrate Drilling Expedition in the Ulleung Basin (UBGH2). Mar Petrol Geol 2013; 47:1-

752        20. https://doi.org/10.1016/j.marpetgeo.2013.07.007.

753    [10] He JX, Zhong CM, Yao YJ, Yan P, Wang YL, Wan ZF, et al. The exploration and productions

754        of gas hydrate and its research progress and exploration prospect in the northern South China

755        Sea. Marine Geology Frontiers 2020; 36 (12): 1-14. http://doi.org/10.16028/j.1009-

756        2722.2020.127.

757 [11] Hovland M, Lysne D, Whiticar M. Gas hydrate and sediment gas composition, Hole 892A. In:

758 Proceedings of the Ocean Drilling Program, Scientific Results. Ocean Drilling Program, Texas

759 A & M University in cooperation with the National Science Foundation and Joint

760 Oceanographic Institutions, Inc; 1995, 146 Part 1. https://doi.org/10.2973/odp.proc.sr.146-

761 1.210.1995.

762 [12] Boswell R, Collett TS, Frye M, Shedd W, McConnell DR, Shelander D. Subsurface gas

763 hydrates in the northern Gulf of Mexico. Mar Petrol Geol 2012; 34(1): 4-30.

764 https://doi.org/10.1016/j.marpetgeo.2011.10.003.

765 [13] Camerlenghi A, Lucchi RG, Rothwell RG. Grain-size analysis and distribution in Cascadia

766 Margin sediments, northeastern Pacific. In: Proceedings of the Ocean Drilling Program,

767 Scientific Results. Ocean Drilling Program, Texas A & M University in cooperation with the

768 National Science Foundation and Joint Oceanographic Institutions, Inc; 1995, 146 Part 1. vol.

769 146. pp. 3–32. https://doi.org/10.2973/odp.proc.sr.146-1.202.1995.

770 [14] von Huene RV, Suess E. Ocean Drilling Program Leg 112, Peru continental margin: Part 1,

771 Tectonic history. Geology 1988; 16 (10): 934–8. https://doi.org/10.1130/0091-

772 7613(1988)016<0934: ODPLPC>2.3.CO;2.

773 [15] Kvenvolden KA, Kastner M. Gas hydrates of the Peruvian outer continental margin. Proc.

774 Ocean Drill. Program Sci. Results 1990; 112: 517–26.

775 https://doi.org/10.2973/odp.proc.sr.112.147.1990.

776 [16] Collett TS, Boswell R, Waite WF, Kumar P, Roy SK, Chopra K, et al. India National Gas

777 Hydrate Program Expedition 02 Summary of Scientific Results: Gas hydrate systems along the

778 eastern continental margin of India. Mar Petrol Geol 2019; 108: 39-142.

779     https://doi.org/10.1016/j.marpetgeo.2019.05.023.

780     [17] Holbrook WS, Hoskins H, Wood WT, Stephen RA, Lizarralde D. Methane hydrate and free gas

781     on the Blake Ridge from Vertical seismic profiling. Science 1996; 273: 1840-3.

782     https://doi.org/10.1126/science.273.5283.1840.

783     [18] Yuan T, Hyndman RD, Spence GD, Desmons B. Seismic velocity increase and deep-sea gas

784     hydrate concentration above a bottom-simulating reflector on the northern Cascadia continental

785     slope. J Geophys Res-Sol Ea 1996; 101:13655-71. https://doi.org/10.1029/96JB00102.

786     [19] Matsushima J. Seismic wave attenuation in methane hydrate-bearing sediments: Vertical

787     seismic profiling data from the Nankai Trough exploratory well, offshore Tokai, central Japan.

788     J Geophys Res-Sol Ea 2006; 111: B10101. https://doi.org/10.1029/2005JB004031.

789     [20] Shankar U, Riedel M. Gas hydrate saturation in the Krishna-Godavari basin from P-wave

790     velocity and electrical resistivity logs. Mar Petrol Geol 2012; 28(10): 1768-78.

791     https://doi.org/10.1016/j.marpetgeo.2010.09.008.

792     [21] Weitemeyer KA, Constable S, Tréhu AM. A marine electromagnetic survey to detect gas

793     hydrate at Hydrate Ridge, Oregon. Geophys J Int 2011; 187(1): 45-62. https://doi.org/

794     10.1111/j.1365-246X.2011.05105.x.

795     [22] Wang XJ, Wu SG, Lee M, Guo YQ, Yang X, Liang JQ. Gas hydrate saturation from acoustic

796     impedance and resistivity logs in the Shenhu area, South China Sea. Mar Petrol Geol 2011;

797     28(9): 1625-33. https://doi.org/10.1016/j.marpetgeo.2011.07.002.

798     [23] Cortes DD, Martin AI., Yun TS, Francisca FM, Santamarina JC, Rupple C. Thermal

799     conductivity of hydrate-bearing sediments. J Geophys Res-Sol Ea 2009; 114: B11103.

800     https://doi.org/10.1029/2008JB006235.

801 [24] Kou X, Li XS, Wang Y, Liu JW, Chen ZY. Heterogeneity of hydrate-bearing sediments:

802 Definition and effects on fluid flow properties. Energy 2021; 229: 120736.

803 https://doi.org/10.1016/j.energy.2021.120736.

804 [25] Wu P, Li YH, Sun X, Liu WG, Song YC. Mechanical characteristics of hydrate-bearing

805 sediment: A review. Energ fuel 2021; 35: 1041-57.

806 https://doi.org/10.1021/acs.energyfuels.0c03995.

807 [26] Cnudde V, Boone MN. High-resolution X-ray computed tomography in geosciences: a review

808 of the current technology and applications. Earth-Sci Rev 2013; 123: 1-17.

809 https://doi.org/10.1016/j.earscirev.2013.04.003.

810 [27] Li CF, Hu GW, Ye YG, Liu CL, Cheng J, Zhang LK, et al. Microscopic distribution of gas

811 hydrate in sediment determined by X-ray computerized tomography. Journal of

812 optoelectronics· Laser 2013; 24(3): 551-7.

813 [28] Yang L, Zhao JF, Liu WG, Li YH, Yang MJ, Song YC. Microstructure observations of natural

814 gas hydrate occurrence in porous media using microfocus X-ray computed tomography. Energ

815 Fuel 2015; 29(8): 4835-41. https://doi.org/10.1021/acs.energyfuels.5b00881.

816 [29] Liang HY, Guan DW, Shi KJ, Yang L, Zhang LX, Zhao JF, et al. Characterizing Mass-Transfer

817 mechanism during gas hydrate formation from water droplets. Chem Eng J 2022; 428: 132636.

818 https://doi.org/10.1016/j.cej.2021.132626.

819 [30] Lv JC, Cheng ZC, Xue KP, Liu Y, Mu HL. Pore-scale morphology and wettability

820 characteristics of xenon hydrate in sand matrix-Laboratory visualization with micro-CT. Mar

821 petrol geol 2020; 120: 104525. https://doi.org/10.1016/j.marpetgeo.2020.104525.

822 [31] Le TX, Bornert M, Aimedieu P, Chabot B, King A, Tang AM. An experimental investigation

823      on methane hydrate morphologies and pore habits in sandy sediment using synchrotron X-ray

824      computed tomography. Mar petrol geol 2022; 122: 104646. https://doi.org/10.1016/j.marpetgeo.2020.104646.

825      https://doi.org/10.1016/j.marpetgeo.2020.104646.

826      [32] Jin Y, Nagao J, Hayashi J, Shimada W, Ebinuma T, Narita H. Observation of Xe hydrate growth

827      at gas-ice interface by microfocus X-ray Computed tomography. J Phys Chem C 2008; 112:

828      17253-6. https://doi.org/10.1021/jp803525m.

829      [33] Lei L, Seol Y, Choi JH, Kneafsey TJ. Pore habit of methane hydrate and its evolution in

830      sediment matrix- Laboratory visualization with phase-contrast micro-CT. Mar Petrol Geol 2019;

831      104: 451-67. https://doi.org/10.1016/j.marpetgeo.2019.04.004.

832      [34] Kou X, Li XS, Wang Y, Liu JW, Chen ZY. Effects of gas occurrence pattern on distribution and

833      morphology characteristics of gas hydrates in porous media. Energy 2021; 226: 120401.

834      https://doi.org/10.1016/j.energy.2021.120401.

835      [35] Yang L, Falenty A, Chaouachi M, Haberthür D, Kuhs WF. Synchrotron X-ray computed

836      microtomography study on gas hydrate decomposition in a sedimentary matrix. G-cubed 2016;

837      17(9): 3717-32. https://doi.org/10.1002/2016GC006521.

838      [36] Gupta A, Moridis GJ, Kneafsey TJ, Sloan ED. Modeling pure methane hydrate dissociation

839      using a numerical simulator from a novel combination of X-ray computed tomography and

840      macroscopic data. Energ Fuel 2009; 23(12): 5958-65. https://doi.org/10.1021/ef9006565.

841      [37] Zhang YC, Liu LL, Wang DG, Zhang Z, Li CF, Meng QG, et al. The interface evolution during

842      methane hydrate dissociation within quartz sands and its implications to the permeability

843      prediction based on NMR data. Mar Petrol Geol 2021; 129: 105065.

844      https://doi.org/10.1016/j.marpetgeo.2021.105065.

845 [38] Kou X, Feng JC, Li XS, Wang Y, Chen ZY. Visualization of interactions between

846     depressurization-induced hydrate decomposition and heat/mass transfer. Energy 2022; 239:

847     122230. https://doi.org/10.1016/j.energy.2021.122230.

848 [39] Rees Emily VL, Kneafsey TJ, Seol Y. Methane hydrate distribution from prolonged and

849     repeated formation in natural and compacted sand samples: X-Ray CT observations. J Geophys

850     Res 2011; 2011: 791815. https://doi.org/10.1155/2011/791815.

851 [40] Ecker C, Dvorkin J, Nur A. Sediments with gas hydrates; internal structure from seismic AVO.

852     Geophysics 1998; 63(5):1659-69.

853 [41] Dai S, Santamarina JC, Waite WF, Kneafsey TJ. Hydrate morphology: Physical properties of

854     sands with patchy hydrate saturation. J Geophys Res-Sol Ea 2012; 117: B11205.

855     https://doi.org/10.1029/2012JB009667.

856 [42] Kou X, Li XS, Wang Y, Wan K, Chen ZY. Pore-scale analysis of relations between seepage

857     characteristics and gas hydrate growth habit in porous sediments. Energy 2021; 218: 119503.

858     https://doi.org/10.1016/j.energy.2020.119503.

859 [43] Helgerud MB, Dvorkin J, Nur A, Sakai A, Collett T. Elastic-wave velocity in marine sediments

860     with gas hydrates: Effective medium modeling. Geophys Res Lett 1999; 26(13): 2021-4.

861     https://doi.org/10.1029/1999GL900421.

862 [44] Berge LI, Jacobsen KA, Solstad A. Measured acoustic wave velocities of R11(CCl3F) hydrate

863     samples with and without sand as a function of hydrate concentration. J Geophys Res-Sol Ea

864     1999; 104(B7): 15415-24. https://doi.org/10.1029/1999JB900098.

865 [45] Dvorkin J, Prasad M, Sakai A, Lavoie D. Elasticity of marine sediments: Rock physics

866     modeling. Geophys Res Lett 1999; 26:1781-4. https://doi.org/10.1029/1999GL900332.

867 [46] Syed FI, Dahaghi AK, Muther T. Laboratory to field scale assessment for EOR applicability in

868      tight oil reservoir. Pet Sci 2022; 19(5): 2131-49. https://doi.org/10.1016/j.petsci.2022.04.014.

869 [47] Collett TS, Johnson AH, Knapp CC, Boswell R, Natural Gas Hydrates: A Review. In: Collett

870      T. Jognson A, Knapp C, Boswel R, editors. Natural Gas Hydrates-Energy Resource Potential

871      and Associated Geologic Hazards, AAPG Mem: Vancouver: American Association of

872      Petroleum Geologists; 2009; 89: 146–219. https://doi.org/10.1306/13201142M891602.

873 [48] Holland M, Schultheiss PJ, Roberts J, Druce M. Observed gas hydrate morphologies in marine

874      sediments, paper presented at 6th International Conference on Gas Hydrates, Chevron,

875      Vancouver, B. C., Canada, 6–10 July, 2008.

876 [49] Wu P, Li YH, Wang L, Sun X, Wu DJ, He XF, et al. Hydrate-bearing sediment of the South

877      China Sea: Microstructure and mechanical characteristics. Eng Geol 2022; 307: 106782.

878      https://doi.org/10.1016/j.enggeo.2022.106782.

879 [50] Liu CL, Meng QG, Hu GW, Li CF, Sun JY, He XL, et al. Characterization of hydrate-bearing

880      sediments recovered from the Shenhu area of the South China Sea. Interpretation-J Sub 2018;

881      5(3): SM13-SM23. https://doi.org/10.1190/INT-2016-0211.1.

882 [51] Liu CL, Meng QG, Li CF, Sun JY, He XL, Yang SX, et al. Characterization of natural gas

883      hydrate and its deposits recovered from the northern slope of the South China Sea. Earth

884      Science Frontiers 2017; 24(4): 41-50.

885 [52] Li CF, Hu GW, Zhang W, Ye YG, Lu CL, Li Q, et al. Influence of foraminifera on formation

886      and occurrence characteristics of natural gas hydrates in fine-grained sediments from Shenhu

887      area, South China Sea. Sci. China Earth Sci 2016; 59: 2223-30. https://doi.org/10.1007/s11430-

888      016-5005-3.

889   [53] Bian H, Qin WX, Luo W, Ma C, Zhu J, Lu C, et al. Evolution of hydrate habit and formation

890      properties evolution during hydrate phase transition in fractured-porous medium. Fuel 2022;

891      324(A): 124436. https://doi.org/10.1016/j.fuel.2022.124436.

892   [54] Badesab F, Dewangan P, Usapkar A, Kocherla M, Peketi A, Mohite K, et al., Controls on

893      evolution of gas-hydrate system in the Krishna-Godavari basin, offshore India, Geochem

894      Geophy Geosy 2017; 18(1): 52-74. https://doi.org/10.1002/2016GC006606.

895   [55] Cha YH, Yun TS, Kim YJ, Lee JY, Kwon TH. Geomechanical, hydraulic and thermal

896      characteristics of deep oceanic sandy sediments recovered during the second Ulleung Basin gas

897      hydrate expedition. Energies 2016; 9(10): 775. https://doi.org/10.3390/en9100775.

898   [56] Liang JQ, Zhang W, Lu JA., Wei JG, Kuang ZG, He YL. Geological occurrence and

899      accumulation mechanism of natural gas hydrates in the eastern Qiongdongnan Basin of the

900      South China Sea: Insights from Site GMGS5-W9-2018. Mar Geol 2019; 418: 106042.

901      https://doi.org/10.1016/j.margeo.2019.106042.

902   [57] Ye JL, Wei JG, Liang JQ, Lu JA, Lu HL, Zhang W. Complex gas hydrate system in a gas

903      chimney, South China Sea. Mar petrol geol 2019; 104: 29-39.

904      https://doi.org/10.1016/j.marpetgeo.2019.03.023.

905   [58] Johnson JE, MacLeod, DR, Phillips, SC, Phyllips MP, Divins DL. Primary deposition and early

906      diagenetic effects on the high saturation accumulation of gas hydrate in a silt dominated

907      reservoir in the Gulf of Mexico. Mar Geol 2022; 444: 106718.

908      https://doi.org/10.1016/j.margeo.2021.106718.

909   [59] Wandrol P, Matějková J, Rek A. High Resolution Imaging by Means of Backscattered Electrons

910      in the Scanning Electron Microscope. Mater Struct Micromech Fract 2008; 567-568: 313–316.

911      https://doi.org/10.4028/www.scientific.net/MSF.567-568.313.

912    [60] Harding DP. Mineral identification using a scanning electron microscope. Miner Metall Proc

913       2002; 19(4):215-9. https://doi.org/10.1007/BF03403272.

914    [61] Bell SK, Joy KH, Pernet-Fisher JF, Hartley ME. QEMSCAN as a method of semi-automated

915       crystal size distribution analysis: Insights from Apollo 15 Mare Basalts. J Petrol 2020; 61(4):

916       egaa047. https://doi.org/10.1093/petrology/egaa047.

917    [62] Gottlieb P, Wilkie G, Sutherland D, Ho-Tun E, Suther S, Perera K, et al. Using quantitative

918       electron microscopy for process mineralogy applications. JoM 2000; 52(4): 24-5.

919    [63] Inkson BJ, Mulvihill M, Mobius G. 3D determination of grain shape in a FeAl-based

920       nanocomposite by FIB-tomography. Scripta Mater 2001; 45:753-8.

921       https://doi.org/10.1016/S1359-6462(01)01090-9.

922    [64] Holzer L, Indutnyi F, Gasser P, Munch B, Wegmann M. Three-dimensional analysis of porous

923       BaTiO3 ceramics using FIB nanotomography. J Microsc 2004; 216: 84-95.

924       https://doi.org/10.1111/j.0022-2720.2004.01397.x.

925    [65] Prill T, Schladitz K. Simulation of FIB-SEM Images for Analysis of Porous Microstructures.

926       Scanning 2013; 35(3)189-195. https://doi.org/10.1002/sca.21044.

927    [66] Chaouachi M, Falenty A, Sell K, Enzmann F, Kersten M, Haberthur D, Kuhs, WF.

928       Microstructural evolution of gas hydrates in sedimentary matrices observed with synchrotron

929       X-ray computed tomographic microscopy. Geochem Geophy Geosy 2015; 16: 1711-22.

930       https://doi.org/10.1002/2015GC005811.

931    [67] Hansen TC, Falenty A, Kuhs WF. Lattice Constants and Expansivities of Gas Hydrates from

932       10 k up to the Stability Limit. J Chem Phys 2016; 144: 054301.

933    https://doi.org/10.1063/1.4940729.

934    [68] Fu XJ, Waite WF, Cueto-Felgueroso L, Juanes R. Xenon hydrate as an analog of methane

935    hydrate in geologic systems out of thermodynamic equilibrium. Geochem Geophy Geosy 2019;

936    20(5):2462-72. https://doi.org/10.1029/2019GC008250.

937    [69] Chen XY, Verma R, Espinoza DN, Prodanovic M. Pore-scale determination of gas relative

938    permeability in hydrate-bearing sediments using X-ray computed microtomography and lattice

939    Boltzmann     method.     Water     Resour     Res     2018;     54(1):     600-8.

940    https://doi.org/10.1002/2017WR021851.

941    [70] Hubbell JH, Seltzer SM. Tables of X-Ray Mass Attenuation Coefficients and Mass Energy-

942    Absorption Coefficients 1 Kev to 20 Mev for Elements Z = 1 to 92 and 48 Additional

943    Substances    of    Dosimetric    Interest.    NIST    Standard    Reference    Database    126.

944    http://physics.nist.gov/PhysRefData/XrayMassCoef/cover.html; 1996, [accessed March 5,

945    2023].

946    [71] Xie YF, Lu JA, Cai HM, Deng W, Kuang ZG, Wang T, et al. The in-situ NMR evidence of gas

947    hydrate forming in micro-pores in the Shenhu area, South China Sea. Energy Rep 2022; 8:

948    2936-46. https://doi.org/10.1016/j.egyr.2022.01.097.

949    [72] Zárate MA. Loess of southern south America. Quat Sci Rev 2003; 22 (18-19): 1987-2006.

950    https://doi.org/10.1016/S0277-3791(03)00165-3.

951    [73] Francisca FM. Evaluating the constrained modulus and collapsibility of loess from standard

952    penetration test. Int J Geomech 2007; 7 (4): 307-10. https://doi/org/10.1061/(ASCE)1532-

953    3641(2007)7:4(307).

954    [74] Rinaldi VA, Rocca RJ, Zeballos ME. Geotechnical characterization and behavior of

955     Argentinean collapsible loess, Character. Eng Prop Natural Soils 2007; 4: 2259-86.

956     [75] Mozejko CA, Francisca FM. Enhanced mechanical behavior of compacted clayey silts

957     stabilized by reusing steel slag. Constr Build Mater 2020; 239: 117901.

958     https://doi.org/10.1016/j.conbuildmat.2019.117901.

959     [76] Liu D, Liao HL, Li YL, Meng QG, Hu GW, Wang JT, et al. Analysis of the mechanical

960     properties of the reconstituted hydrate-bearing clayey-silt samples from the South China Sea. J

961     Mar Sci Eng 2022; 10(6): 831. https://doi.org/10.3390/jmse10060831.

962     [77] Makogon YF, Holditch SA, Makogon TY. Natural gas-hydrates-A potential energy source for

963     the 21st Century. J Pet Sci Eng 2007; 56(1-3): 14-31.

964     https://doi.org/10.1016/j.petrol.2005.10.009.

965     [78] Makogon YF, Omelchenko RY. Commercial gas production from Messoyakha deposit in

966     hydrate conditions. J Nat Gas Sci Eng 2013; 11:1-6.

967     https://doi.org/10.1016/j.jngse.2012.08.002.

968     [79] Toumelin E, Torres-Verdin C, Chen S. Modeling of multiple echo-time NMR measurements

969     for complex pore geometries and multiphase saturations. SPE Reserv Eval Eng 2003; 6(04):

970     234-43. https://doi.org/10.2118/85635-PA.

971     [80] Toumelin E, Torres-Verdín C, Sun B, Dunn KJ. Random-walk technique for simulating NMR

972     measurements and 2D NMR maps of porous media with relaxing and permeable boundaries. J

973     Magn Reson 2007; 188(1): 83-96. https://doi.org/10.1016/j.jmr.2007.05.024.

974     [81] Provis JL, Myers RJ, White CE, Rose V, van Deventer JSJ. X-ray microtomography shows

975     pore structure and tortuosity in alkali-activated binders. Cem Concr Res 2012; 42: 855-64.

976     https://doi.org/10.1016/j.cemconres.2012.03.004.

977 [82] Bird MB, Butler SL, Hawkes CD, Kotzer T. Numerical modeling of fluid and electrical currents

978 through geometries based on synchrotron X-ray tomographic images of reservoir rocks using

979 Avizo and COMSOL. Comput Geosci 2014; 73: 6–16.

980 https://doi.org/10.1016/j.cageo.2014.08.009.

981 [83] Liu XJ, Zhu HL, Liang LX. Digital rock physics of sandstone based on micro-CT technology.

982 Chin J Geophys Ed 2014; 57: 1133–40. https://doi.org/10.6038/cjg20140411.

983 [84] Childs EC. Dynamics of fluids in porous media. Eng Geol 1972; 7: 174-5.

984 https://doi.org/10.1016/0013-7952(73)90047-1.

985 [85] Wu SH, Cai ZQ, Shi SM. Oil Deposit Geology. Beijing: Petroleum Industry Press; 2011.

986 [86] Chen RS. Petroleum and Gas Geology. Wuhan. China University of Geosciences Press Co.,

987 LTD; 1994.

988 [87] Staykova DK, Kuhs WF, Salamatin AN, Hansen T. Formation of porous gas hydrates from ice

989 powders: Diffraction experiments and multistage model. J Phys Chem B 2003; 107: 10299.

990 https://doi.org/10.1021/jp027787v.

991 [88] Lei L, Santamarina JC. Laboratory strategies for hydrate formation in fine-grained sediments.

992 J Geophys Res-Sol Ea 2018; 123: 2583–96. https://doi.org/10.1002/2017JB014624.

993 [89] Wang L, Li YH, Shen S, Liu WG, Sun X, Liu Y, et al. Mechanical behaviors of gas hydrate-

994 bearing clayey sediments of the South China Sea. Environ Geotech 2022; 9(4): 210-22.

995 https://doi.org/10.1680/jenge.19.00048.

996 [90] Liu Z, Kim J, Lei L, Ning FL, Dai S. Tetrahydrofuran hydrate in clayey sediments-laboratory

997 formation, morphology, and wave characterization. J Geophys res-Sol Ea 2019; 124(4): 3307-

998 19. https://doi.org/10.1029/2018JB017156.

999  [91] Sun JX, Ning FL, Wu NY, Li S, Zhang K, Zhang L, et al. The effect of drilling mud properties

1000  on shallow lateral resistivity logging of gas hydrate bearing sediments. J Petrol Sci Eng 2015;

1001  127: 259-69. https://doi.org/10.1016/j.petrol.2014.12.015.

1002  [92] Jiang M, Zhu F, Utili S. Investigation into the effect of backpressure on the mechanical behavior

1003  of methane-hydrate-bearing sediments via DEM analyses. Comput Geotech 2015; 69: 551–63.

1004  https://doi.org/10.1016/j.compgeo.2015.06.019.

1005  [93] Lee JY, Jung JW, Lee MH, Bahk JJ, Choi J, Ryu BJ, et al. Pressure core study of gas hydrates

1006  in the Ulleung Basin and implication for geomechanical controls on gas hydrate occurrence.

1007  Mar petrol geol 2013; 47: 85-98. https://doi.org/10.1016/j.marpetgeo.2013.05.021.

1008  [94] Konrad JM, Morgenstern NR. Effects of applied pressure on freezing soils. Can Geotech J 1982;

1009  19: 494-505. https://doi.org/10.1139/t82-053.

1010  [95] Nixon JF. Discrete ice lens theory for frost heave in soils. Can Geotech J 1991; 28: 843-59.

1011  https://doi.org/10.1139/t91-102.

1012  [96] Chen F, Su X, Lu HF, Zhou Y. Relations between biogenic component (foraminifera) and highly

1013  saturated gas hydrates distribution from Shenhu Area, northern South China Sea. Earth science-

1014  journal of China University of Geosciences 2013; 38(5):907-15.

1015  https://doi.org/10.3799/dqkx.2013.089

1016  [97] Berge LI, Jacobsen KA, Solstad A. Measured acoustic wave velocities of R11(CCl3F) hydrate

1017  samples with and without sand as a function of hydrate concentration. J Geophys Res 1999;

1018  104(B7): 15415-24. https://doi.org/10.1029/1999JB900098.

1019  [98] Li J, Lu JA, Kang DJ, Ning FL, Lu HF, Kuang ZG, et al. Lithological characteristics and

1020  hydrocarbon gas sources of gas hydrate-bearing sediments in the Shenhu Area, South China sea

1021    Implications from the W01B and W02B sites. Mar Geol 2019; 408: 36-47.

1022    https://doi.org/10.1016/j.margeo.2018.10.013.

1023    [99] Myerson AS. Handbook of Industrial Crystallization, 2nd ed. Boston: Butterworth-Heinemann;

1024    2002.

1025    [100] Shimada N, Sugahara K, Sugahara T, Ohgaki K, et al. Phase transition from structure-H to

1026    structure-I in the methylcyclohexane plus xenon hydrate system. Fluid Phase Equilibr 2003;

1027    205(1): 17-23. https://doi.org/10.1016/S0378-3812(02)00186-3.

1028    [101] Mullin JW. Crystallization. 3rd ed. Oxford: Butterworth-Heinmann; 2001.

1029    [102] Park T, Lee JY, Kwon TH. Effect of pore size distribution on dissociation temperature

1030    depression and phase boundary shift of gas hydrate in various fine-grained sediments. Energ

1031    Fuel 2018; 32(4): 5321-30. https://doi.org/10.1021/acs.energyfuels.8b00074.

1032    [103] Liu CL, Ye YG, Sun SC, Chen Q, Meng QG, Hu GW. Experimental studies on the P-T stability

1033    conditions and influencing factors of gas hydrate in different systems. Sci China Earth Sci 2003;

1034    56(4): 594-600. https://doi.org/10.1007/s11430-012-4564-3.

1035    [104] Ben Clennell M, Hovland M, Booth JS, Henry P, Winters WJ. Formation of natural gas

1036    hydrates in marine sediments 1. Conceptual model of gas hydrate growth conditioned by host

1037    sediment properties. J Geophys Res-Sol Ea 1999; 104(No.B10): 22985-3003.

1038    https://doi.org/10.1029/1999JB900175.

1039    [105] Yang MJ, Song YC, Liu Y. Effects of porous media and salinity on phase equilibrium of

1040    methane hydrates. Jounral of Dalian University of Technology 2011; 51(1): 31-35.

1041    [106] Xie Y, Zheng T, Zhong JR, Zhu YJ, Wang YF, Zhang Y, et al. Experimental research on self-

1042    preservation effect of methane hydrate in porous sediments. Appl Energ 2020; 268: 115008.

1043      https://doi.org/10.1016/j.apenergy.2020.115008.

1044    [107] Bai DS, Zhang DW, Zhang XR, Chen GJ. Origin of self-preservation effect for hydrate

1045      decomposition: Coupling of mass and heat transfer resistances. Sci Rep-UK 2015; 5:14599.

1046      https://doi.org/10.1038/srep14599.

1047    [108] Schlüter S, Sheppard A, Brown K, Wildenschild D. Image processing of multiphase images

1048      obtained via X-ray microtomography: a review. Water Resour Res 2014; 50(4): 3615–39.

1049      https://doi.org/10.1002/2014WR015256.

1050    [109] Liu Y, Zhang W, Liang XL, Zu L, Tang XY. Determination on representative element volume

1051      of Nanjing silty-fine sand for its spatial pore structure. Rock and Soil Mechanics 2019; 40(7):

1052      2723-9.